ESA Contract: "Maintenance and Update of the European Mars Climate Database"

Ref: ESA Contract No. 4000117944/16/NL/LF/as

Improved LMD Global Climate Model implementation report.

Part 1: Improved dust cycle

Work Package 4

Prepared by: Ehouarn Millour, Margaux Vals, Chao Wang, Déborah Bardet, Francois Forget, Aymeric Spiga

Laboratoire de Météorologie Dynamique, CNRS, IPSL, Paris, France.

January 12, 2018

Contents

1 Introduction

This document reviews the work carried at LMD to improve the vertical distribution of atmospheric dust in the LMD Mars Global Climate Model (GCM) and, in particular, the parametrization of **detached dust layers** in the GCM.

The origin of the detached dust layers observed by the Mars Climate Sounder (MCS) aboard the Mars Reconnaissance Orbiter (MRO) is still debated. *Spiga et al.* [2013] revealed that deep mesoscale convective "rocket dust storms" are likely to play an important role in forming these dust layers. The first sections of this document focuse on the design of a parametrization of these "rocket dust storms" in the LMD Martian GCM, developped by Chao Wang during its PhD at the LMD. The new parameterization allows dust particles in the GCM to be transported to higher altitudes than in traditional GCMs. Combined with the horizontal transport by large-scale winds, the dust particles spread out and form detached dust layers.

During the Martian dusty seasons, the LMD GCM with the new parameterization is able to form detached dust layers. The formation, evolution and decay of the simulated dust layers are largely in agreement with the MCS observations. This suggests that mesoscale rocket dust storms are among the key factors to explain the observed detached dust layers on Mars. However, the detached dust layers remain absent in the GCM during the clear seasons, even with the new parameterization. This implies that other relevant atmospheric processes, operating when no dust storms are occurring, are needed to explain the Martian detached dust layers. This is what the second section is about: a new parametrization, completing the previous one and also initiated by Chao Wang during its PhD at the LMD, aiming at representing the dust lifted by slope winds converging over the high topography during daytime.

Another aspect of improvement of the parametrization of detached dust layers relies on the dust injection scheme. The third section of this document describes the work carried on a new scheme of dust injection by Daborah Bardet during her internship at LMD. In this scheme, the local columnar amount of dust is no longer strictly imposed by a forcing scenario (i.e. normalization of the column optical depth at all times to match values provided by a dust scenario), but realistically and adequately injected over the day to reach a target value provided by the dust scenario.

2 Parametrization of detached dust layers triggered by rocket dust storms

2.1 Introduction

Airborne dust is a crucial component of the Martian climate system. It affects the Martian atmosphere's radiative balance by absorbing and scattering short-wave solar radiation, as well as absorbing and emitting long-wave infrared radiation. It has a strong impact on Martian meteorology and climate.

The vertical distribution of dust constrains our understanding of the Martian dust cycle. For a long time, taking into consideration the combined effects of gravitational sedimentation and vertical mixing, dust has been assumed to be well-mixed in the lower atmosphere up to a level in the troposphere, and to decrease as a function of pressure above this level [*Conrath*, 1975; *Forget et al.*, 1999]. However, this assumption is challenged by the observations of the Mars Climate Sounder (MCS) instrument aboard the Mars Reconnaissance Orbiter (MRO) [*McCleese et al.*, 2007]. MCS demonstrated the year-round existence of detached dust layers in the middle troposphere of Mars. These detached dust layers are characterized by mass mixing ratio maxima at 15-25 km ($\sim$60-120 Pa on Mars), which is above the planetary boundary layer (PBL), during Martian clear seasons (northern spring and summer). The dust concentration in these maxima can be 2-10 times larger than the concentration near the surface [*McCleese et al.*, 2010; *Heavens et al.*, 2011a,b,c]. During Martian dusty seasons (northern autumn and winter), the detached dust layers appear to have higher altitude and concentration. Meanwhile, their height and concentration also vary significantly in these seasons (See Figures 10 and 11 in *McCleese et al.* [2007]). The detached dust layers observed by MCS are mainly distributed over tropical latitudes, with high detached layers over the poles in the summer hemisphere. The longitudinal variability of the detached dust layers is relative weak [*Heavens et al.*, 2014]. This detached dust layer phenomenon has been confirmed directly by limb observations using the Thermal Emission Spectrometer (TES) on the Mars Global Surveyor (MGS) [*Guzewich et al.*, 2013] and the Compact Reconnaissance Imaging Spectrometer for Mars (CRISM) onboard MRO [*Smith et al.*, 2013], and possibly by radio-occultations with the Spectroscopy for the Investigation of Characteristics of the Atmosphere of Mars (SPICAM) instrument on Mars Express [*Määttänen et al.*, 2013]. The detached dust layers have also been indirectly identified by their thermal signature in MCS data [*Navarro et al.*, 2014a].

The origin of the detached dust layers phenomena remains uncertain.

Dust storms, ranging from local, regional and planet-encircling scale, are regularly observed on Mars, with the largest storms occurring from southern spring to summer (often termed the "dust storm season") [*Cantor et al.*, 2001; *Cantor*, 2007; *Wang and Richardson*, 2015]. Many types of regional and larger storms, resulting from lifting over large areas, have been numerically modeled in traditional GCMs [*Newman et al.*, 2002; *Basu et al.*, 2004, 2006; *Kahre et al.*, 2006; *Mulholland et al.*, 2013, 2015; *Newman and Richardson*, 2015]. In some of these simulations, dust with detached structures are simulated, for instance, in *Newman et al.* [2002]. However, comparing to the MCS observed detached dust layers, the resulting dust layers in their studies are, first, not as opaque as the MCS observed ones [*Heavens et al.*, 2011a]. Second, the simulated dust layers are short-lived compared to the MCS observations. The aloft dust sediments as the storms dissipate. While in MCS data, detached dust layers remain for longer time period and also exist outside the dust storm seasons. Moreover, the detached dust layers are observed in the tropics during most of northern spring and summer by MCS [*Heavens et al.*, 2011a], yet large dust storms are rarely observed during this period [*Cantor et al.*, 2001].

What can explain the observed departure from a vertically well-mixed atmosphere? Several mechanisms have been proposed.

Firstly, small-scale dust devils are suspected to be the dominant phenomena maintain-

ing the atmospheric dust loading during the northern spring and summer [*Kahre et al.*, 2006]. *Heavens et al.* [2011a] evaluated their capacity to lift dust particles into the high atmosphere, and the results suggested that dust devils can not create detached dust layers as high as observed. The observed heights of dust devils are not higher than $\sim$8 km [*Fisher et al.*, 2005], which is much lower than the typical height of MCS-observed detached dust layers.

Secondly, scavenging of dust by water ice particles could also explain the formation of the detached dust layers [*Heavens et al.*, 2011a]. In water ice clouds, ice crystals grow onto dust particles (heterogeneous nucleation). The increase of a dust particle's mass enhances its sedimentation velocity. When the particles sediment to a level where the temperature is higher than the condensation temperature, ice sublimes and dust concentration below the ice cloud is enriched, hence forming a detached dust layer. This scavenging process has been elaborately parameterized in the Martian Global Climate Model (GCM) developed at the Laboratoire de Météorologie Dynamique (LMD) [*Navarro et al.*, 2014b]. It was found that dust scavenging by water ice alone fails to reproduce detached dust layer observed by MCS.

Overall, so far, all endeavors to model dust lifting in a traditional GCM fail to reproduce the MCS observed detached dust layers. The radiative heating of the dust does not create detached layers except for the case of "solar escalator" [*Daerden et al.*, 2015]. The detached dust layers observed by the light detection and ranging (LIDAR) instrument on the Phoenix Lander were simulated with the Global Environmental Multiscale model for Mars by *Daerden et al.* [2015]. In their simulation, the surface dust is lifted into the atmosphere due to large wind shear. And the heating of the dust by solar radiation causes buoyant instability and mixing across the top of the PBL. In the following sols (one sol means one Martian day), solar heating of the dust causes it to "escalate" slowly, leading to a detached dust layer remaining in the troposphere. This study highlights the fact that solar heated dust layers tends to be lifted and could create detached layers on Mars. However, in most case when modeled at GCM scales, it seems that in general this process cannot create all the detached dust layers observed on Mars.

In contrast with coarse-resolution GCMs, however, dust clouds are subjected to strong vertical convective motion in fine-resolution mesoscale models. Two processes detailed below have been explored to simulate dust vertical motion in Martian mesoscale models, i.e., slope winds [*Rafkin et al.*, 2002] and "rocket dust storms" [*Spiga et al.*, 2013]. In both cases, dust layers, resembling the MCS-like detached dust layers, could be produced.

The thermally-driven slope winds on Mars can be 2.5 times stronger than those on Earth under similar conditions [*Ye et al.*, 1990; *Spiga*, 2011]. The daytime upslope flow blows dust from the bottom to the top of a mountain, continues to raise up above the mountain top and diverges horizontally at high altitudes. Thus, an orographic circulation is produced. This specific circulation around the volcano Arsia Mons was simulated by *Rafkin et al.* [2002] with the Mars Regional Atmospheric Modeling System. In their simulation, a "spiral dust cloud" formed at an altitude of $\sim$20 km, which implies that the dust lifted and transported by slope winds is capable of penetrating beyond the PBL and forming a detached dust layer. The height of the spiral cloud resembled that of the observed detached dust layers. In addition, by investigating the MCS-observed extreme detached dust layers outside of regional and global dust storms over Olympus Mons and the Tharsis Montes, *Heavens et al.* [2015] explored how the MCS observations are connected to the mesoscale orographic circulation. *Heavens et al.* [2015] also found that the vertical mixing caused by the orographic circulation could be even stronger than *Rafkin et al.* [2002]'s simulation.

A "rocket dust storm", using terminology originally proposed by *Spiga et al.* [2013], is a storm which can raise dust particles rapidly and efficiently to high altitudes in the Martian troposphere (30-50 km). *Spiga et al.* [2013] showed that, after lifting and during daytime, the evolution of any low-level local dust storm of sufficiently high opacity will be governed by deep mesoscale convective motions driven by dust solar heating. Combined with the strong large-scale horizontal winds, the dust particles, lifted to high altitudes, are then

spread horizontally to form a detached dust layer. Due to the nocturnal sedimentation of dust, which is less efficient compared to the daytime deep convection, and due to the further radiatively-induced convection that occurs on the following sol, the detached dust layer remains stable for several Martian sols. A rocket dust storm can therefore be a plausible origin of detached dust layers. However, it is not possible for a GCM to directly represent this process because the rocket dust storm motions occur at scales that are finer than a traditional GCM's horizontal resolution. As *Spiga et al.* [2013] pointed out, to further explore the origins of the MCS-observed detached dust layers as well as the interactions between dust and other atmospheric components, it is necessary to parameterize the mesoscale deep convection, which is a robust process missing in any Martian global climate model. Such a parameterization is also necessary to investigate the global and seasonal variabilities of detached dust layers on Mars, which is too difficult to perform with the mesoscale models.

In this paper, our objective is to parameterize the rocket dust storms in a Martian GCM to explore the role of mesoscale dust convection in forming the detached dust layers on Mars. To do so, a new subgrid parameterization for rocket dust storms to represent the mesoscale dust convection is designed and implemented in the LMD Martian GCM, and tested in simulations in which dust injection from the surface is simply assumed when the dust opacity is measured to significantly increase in the available observed dust climatology. A brief general description of the LMD Martian GCM can be found in section 2. The parameterization is detailed in section 3. In section 4, results and sensitivity studies are presented. The simulated dust vertical structures are then compared to the MCS observations (section 5). In the last section, we state the conclusions of this study.

2.2 The LMD Martian GCM

The LMD Martian GCM was originally developed in the early 1990s. It is composed of a grid-point dynamic core, integrating the hydrodynamic equations with a finite difference method, and a comprehensive set of physical packages taking into account radiative transfer [*Forget et al.*, 1999], dust cycle [*Madeleine et al.*, 2011], water cycle [*Montmessin et al.*, 2004; *Madeleine et al.*, 2012; *Navarro et al.*, 2014b], planetary boundary layer mixing [*Colaïtis et al.*, 2013] and other physical processes (see details in *Forget et al.* [1999] and *Forget et al.* [2011]).

On Mars, the main radiative agents are gaseous CO_2 and aerosols, i.e., airborne dust and water ice. For CO_2, a wide-band model is adopted in the GCM to accurately simulate the emission and absorption of radiation in the 15-μm bands [*Hourdin*, 1992]. The Doppler effect, the broadening of CO_2 molecular lines at low pressure, and non-local thermal equilibrium (NLTE) are also included. In the near-infrared bands of CO_2, atmospheric heating due to the absorption of solar radiation is parameterized [*Forget et al.*, 1999]. The radiative effect of dust particles is included in the radiative transfer equations, particularly the multiple scattering by dust particles outside the CO_2 15-μm bands. The radiative properties of dust particles from *Wolff et al.* [2006, 2009] are used as the most accurate dust scattering properties published to date.

Dust is described in the GCM by using a semi-interactive scheme [*Madeleine et al.*, 2011]. It is constantly injected from the surface at all time and all places. The shape of the vertical profile of dust is free to evolve through transport, mixing and sedimentation, but the total column dust optical depth (CDOD) in the GCM is rescaled to a daily observation-based CDOD map (also called prescribed dust scenario) [*Montabone et al.*, 2015]. This transport scheme allows a better representation of the dust distribution. The transport of dust is represented by a two-moment scheme [*Madeleine et al.*, 2011]. The two moments are, respectively, the mass mixing ratio and the number mixing ratio. The advection of each moment is implemented separately. By assuming a log-normal size distribution, the effective radius of dust particles can be computed. The optical properties of the dust, such as opacity, extinction coefficient and optical depth, can thus be obtained.

2.3 Modeling strategy for the rocket dust storm parameterization

The objective of this parameterization is to represent the mesoscale dust convection inducing rocket dust storm in the GCM, so that the dust will not only mix in the lower part of the troposphere (as assumed before), but also get injected up to high altitudes as predicted in mesoscale models. Owing to convective motions, the main difficulty in this parameterization, as explained above, is that the rocket dust storm happens at scales smaller than the GCM's horizontal resolution, which is typically ∼250 km. In order to better represent the real size of the rocket dust storm, subgrid scale convective motion induced by radiative heating of dust must be represented.

In practice, we assume that a fraction of a horizontal grid cell is occupied by the local storm, and the rest only contains the usual environment dust present before the local dust storm event occurs. Two distinct dust tracers (transported by resolved motions in the GCM) are thus used in the rocket dust storm parameterization, i.e., the "environment dust" and the "storm dust". The results from mesoscale simulations of the rocket dust storm [*Spiga et al.*, 2013] are used to calibrate this parameterization.

2.3.1 Trigger assumption

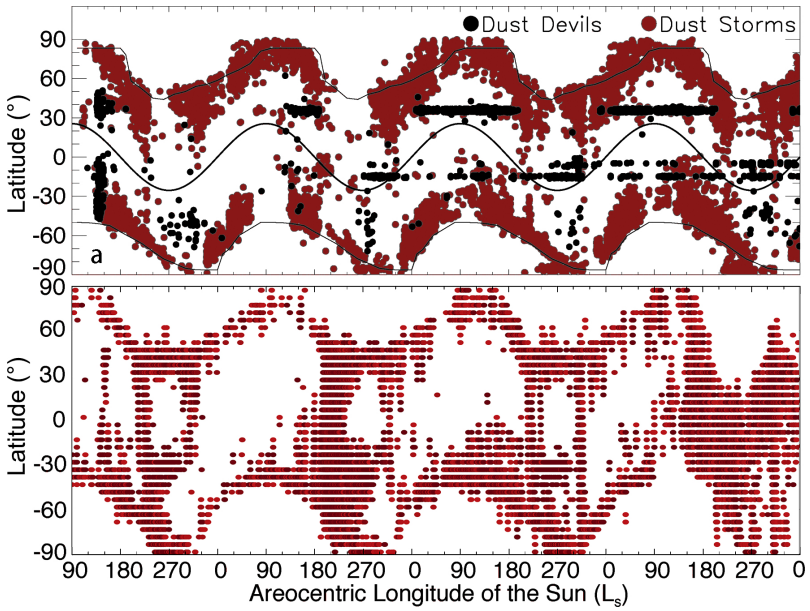

Figure 1: (a) Latitudinal distribution of Martian dust devils and storms versus areocentric longitude of the sun, from MY24 to MY27 (adapted from *Cantor et al.* [2006]). (b) Dust storms identified from the prescribed dust scenarios [*Montabone et al.*, 2015] where CDOD changes larger than 0.2 per sol are observed during the same time period. Note that the cluster of dust storms in MY25 is associated with the global dust storm.

As mentioned before, the CDOD in the GCM is driven by a prescribed dust scenario derived from observations. In the parameterization, the onset of a dust storm is thus implemented in a grid point when a sufficiently large CDOD increase ($\Delta\tau_{dust}$) is detected. When $\Delta\tau_{dust}$ in one GCM grid point between one sol and the next is greater than 0.2, we assume that a significant dust storm occurred and that strong mesoscale deep convection would have occurred also, thus the parameterization should be triggered. This strategy is based on the assumption that the dust particles lifted by a rocket dust storm will result in a rapid and large increase of dust optical depth. By setting this criterion ($\Delta\tau_{dust} > 0.2$),

we found that the set of dust storms triggered by the GCM is comparable to the observed ones from *Cantor et al.* [2006] (See Figure 1). In particular, some storms are obtained around the polar caps in northern summers and winters. In the equatorial regions, several storms are obtained during the dusty seasons, while almost no storm is obtained during the clear seasons. Besides, the criterion is also helpful to improve computational efficiency. In the meantime, below this criterion, injecting smaller amount of dust produce weak response which is negligible in GCM. In this study, the trigger of the dust storms, which are observed by satellites, is different to the mechanisms based on the local meteorological conditions, such as near-surface wind stress and convective vortices. However, there are differences in the locations and frequencies of the identified dust storms from GCM dust scenarios and *Cantor et al.* [2006]'s study. Such as, in the dusty season of MY27, more dust events are identified in the dust scenario than those in *Cantor et al.* [2006]'s study. The possible cause may be that, from the Fig. 21 in *Montabone et al.* [2015], three dusty periods are found in MY 27, around Ls 150°, 230° and 320°. But from MY24 to MY26, there are only one or two dusty periods. Thus, dust optical depth varies more in MY27 than in the other three Martian years, which results more dust events in GCM. The discrepancy may also hint that the threshold of $\Delta\tau_{dust}$ is not uniform at all places and time. It could be location- and/or season-dependent. The differences could also result from some of the dust storms identified by *Cantor et al.* [2006] not being rocket dust storms (i.e. by some storms having $\Delta\tau_{dust} \leq 0.2$ per sol). Additionally, when large-scale dust storms (with $\Delta\tau_{dust} > 0.2$) occur, they are treated as an ensemble of adjacent rocket dust storms.

2.3.2 Dust injection

During the daytime, the amount of dust lifted by the storm is directly associated with radiative warming in the rocket dust storm. The dust optical depth in each layer of pressure thickness dp is given by:

$$\mathrm{d}\tau_{dust} = \frac{3}{4}\frac{Q_{ext,\lambda}\, q}{\rho_{dust}\, r_{eff}\, g}\,\mathrm{d}p \tag{1}$$

where $Q_{ext,\lambda}$ is the dust extinction coefficient at a given wavelength λ, q is the mass mixing ratio of the dust (kg/kg), ρ_{dust} is the density of dust particle (2500 kg/m^3), r_{eff} is the effective radius of dust particle, and g is the Martian gravitational acceleration. For a given sol-to-sol increase $\Delta\tau_{dust}$, the flux of lifted dust ν_{lift} (kg m^{-2} s^{-1}) can be estimated by:

$$\nu_{lift} = \frac{4}{3}\frac{\Delta\tau_{dust}\, \rho_{dust}\, r_{eff}}{\Delta t\, Q_{ext,\lambda}} \tag{2}$$

with Δt the duration of the lifting per sol (s).

The dust injection from the surface into the atmosphere is only performed in the morning, from Martian local time (LT) 10:00 (t_{start}) to 12:00 (t_{end}) (in Equation 2, $\Delta t = (t_{end} - t_{start}) * 88775/24$). t_{start} and t_{end} are chosen empirically. The best match among GCM simulations, mesoscale simulations and observations is reached by activating dust lifting in this local time range (see text in section 2.4.5). The goals of the best match have two aspects. First, for each individual rocket dust storm, the vertical convection (such as the magnitude of the vertical velocity and the height reached) of the storm should behave similarly to those in the mesoscale studies. Second, the annual simulated vertical dust distribution should be as close as possible to the MCS observations, i.e. the formation of the detached dust layers and the variation/evolution of the heights of the detached dust layers over the simulated Martian year.

After the onset of dust storm, an estimation of the fractional area occupied by the local dust storm within the GCM grid cell is needed. The maximum optical depth of the OMEGA local dust storm studied by *Spiga et al.* [2013] and *Määttänen et al.* [2009] is $\sim$10, extending over one scale height above the surface (i.e. $\Delta p \approx 200Pa$). By assuming

an extinction coefficient of 2.4, effective radius of 2 μm, and dust particle density of 2500 kg/m^3, a corresponding reference mass mixing ratio can be computed through

$$q_{ref} = \frac{4}{3} \frac{\rho_{dust}\, r_{eff}\, g}{Q_{ext,\lambda}\, \Delta p}\, \tau \tag{3}$$

which gives q_{ref}=5$\times$10^{-4} kg/kg. By comparing the mass mixing ratio of the lifted storm dust spread over the entire grid cell to this reference value, i.e. assume the optical depth for all the local dust storms is 10, the areal fraction of the GCM grid occupied by the local storm can be estimated. If the mass mixing ratio of the grid is larger than or equal to q_{ref}, the fraction is set equal to 1.

For the sake of comparison between model outputs and existing diagnostics of MCS dust observations, the density-scale opacity is employed to describe dust distributions. It can be written as

$$\frac{\mathrm{d}\tau_{dust}}{\rho} = \frac{3}{4} \frac{Q_{ext,\lambda}}{\rho_{dust}\, r_{eff}} q \tag{4}$$

where ρ is the air density. This quantity is proportional to the dust mass mixing ratio and the aerosol heating rates [*Heavens et al.*, 2010; *Spiga et al.*, 2013].

2.3.3 Radiative transfer

After the onset of a rocket dust storm, at each timestep, the radiative transfer calculations are performed twice in a row. The first radiative transfer iteration is calculated with only environment dust. This gives the environmental heating rate $(\frac{\mathrm{d}T}{\mathrm{d}t})_{env}$ (T is temperature) outside the dust storm. The second radiative transfer iteration features both the environment dust and the storm dust, which gives the heating rates $(\frac{\mathrm{d}T}{\mathrm{d}t})_{storm+env}$ inside the dust storm. The radiative effect due to the presence of the rocket dust storm (named "extra heating" hereafter, $\Delta\mathcal{H}$) can be obtained by:

$$\Delta\mathcal{H} = (\frac{\partial T}{\partial t})_{storm+env} - (\frac{\partial T}{\partial t})_{env} \tag{5}$$

2.3.4 Vertical transport

Spiga et al. [2013] demonstrated through mesoscale modeling that the ascent of a rocket dust storm is controlled by the competing radiative warming and adiabatic cooling. In the parameterization we therefore assume that the extra heating $\Delta\mathcal{H}$ due to the presence of the storm dust is completely balanced by adiabatic cooling through vertical motion. From the Eulerian point of view, potential temperature for each layer in the GCM is modified by the adiabatic process, which is:

$$\frac{\partial\theta}{\partial t} = \Delta\mathcal{H}\, \Pi^{-1} - w\, \frac{\mathrm{d}\theta}{\mathrm{d}z} \tag{6}$$

where w is the vertical velocity inside the storm, z is altitude, θ is the potential temperature of air, and Π is the Exner function:

$$\Pi = \left(\frac{P}{P_0}\right)^{\frac{R}{c_p}} \tag{7}$$

where P is the pressure, P_0 is the reference pressure, R is the gas constant, and c_p is the specific heat capacity. By considering that the radiative warming is balanced by the vertical motion,

$$\frac{\partial\theta}{\partial t} = 0 \tag{8}$$

Assuming the condition of hydrostatic equilibrium, the vertical velocity w can be written as

$$w = \frac{\Delta\mathcal{H}}{\frac{\mathrm{d}T}{\mathrm{d}z} + \frac{g}{c_p}} \tag{9}$$

where c_p is the specific heat capacity. This equation leads to a comparable magnitude of vertical velocity in the GCM to the one simulated in the mesoscale models [*Rafkin*, 2009, 2012; *Spiga et al.*, 2013]. The values of the vertical velocities within the rocket dust storm are about two orders of magnitude larger than the typical vertical velocities in GCM simulations ($\sim$0.1 m/s).

After estimation of the vertical velocity, in the subgrid region where the rocket dust storm begins, the storm dust tracer is vertically advected in the parameterization by a Van Leer transport scheme [*Van Leer*, 1977; *Hourdin and Armengaud*, 1999]. The environmental dust is not involved in this vertical convection. Note that after the vertical transport, the subgrid storm dust is averaged over the whole grid cell and this value is used in other GCM computations that require knowledge of dust abundance. For each timestep during the simulation, the storm dust is also transported by large-scale motions in the GCM, such as the Hadley cell, which is typically strengthened due the enrichment of dust.

2.3.5 Detrainment of storm dust

Once transferred to high altitude, if the velocity of the storm dust decreases, the storm dust starts to detrain into environment dust. This process represents the effects of dilution and mixing of the storm dust, and how dust injected into the atmosphere by dust storms replenishes the ambient veil of dust particles on Mars. The detrainment of storm dust is a key process in this parameterization, because it controls the amount of storm dust remaining in the convective storm, thus the radiative heating rate $\Delta\mathcal{H}$ imposed by this storm. It is worth noting that when the convection of the triggered dust storm is not deep enough, it is possible that the dust storm will dissipate before penetrating the PBL. Mixing process (i.e. entrainment and detrainment) in cumulus convection on Earth has been parameterized by various methods [*de Rooy et al.*, 2013]. For deep convection, LES simulations show that variations of mass flux are determined by detrainment, rather than entrainment [*de Rooy and Siebesma*, 2010; *Böing et al.*, 2012]. An analytical expression for detrainment, in term of buoyancy, vertical velocity and cloud fraction, is given by *de Rooy and Siebesma* [2010] (see Equation 28 in their study) for terrestrial cumulus convection. But unlike the Earth case, there are few studies exploring the fine-scale entrainment/detrainment on Mars. In this study, during the ascent of a storm, the effect of the buoyancy (alternatively, the extra heating) and the fraction of the local storm can be represented by the vertical velocity to some extent (see Equation 9). Combine with the fact that a deeper dust layer will form given a smaller detrainment rate, for the sake of simplicity, a function is defined by assuming that the coefficient of detrainment is inversely dependent on the vertical velocity of the storm dust (shown in Figure 2), i.e., the lower the velocity of storm dust is, the more efficient the detrainment is.

2.3.6 Horizontal transportation and sedimentation

The motion of the storm is also controlled by the large scale horizontal winds from the dynamics of the GCM. It becomes particularly obvious after the rocket dust storm penetrates beyond the PBL.

During the nighttime, the storm dust loses its convective energy (solar energy). It sediments for two reasons. The first is gravity. According to Stokes's law, the terminal velocity of dust is proportional to the effective radius of the particle. In a rocket dust storm, it is modeled that the effective radius of the dust particles is larger than that of the environment dust because of the strong vertical wind that transported up the rocket dust storm. The sedimentation for storm dust will therefore be more efficient than for environment dust. The second reason is that the dusty air parcel (dust storm) radiates more energy in the infrared bands than its environment, which results in a negative $\Delta\mathcal{H}$ during the night. Based on the equation 5 and 9, which are applied at all time in the GCM, the velocities of the dust particles in the storm become negative (i.e., downward). This supports the downward motion

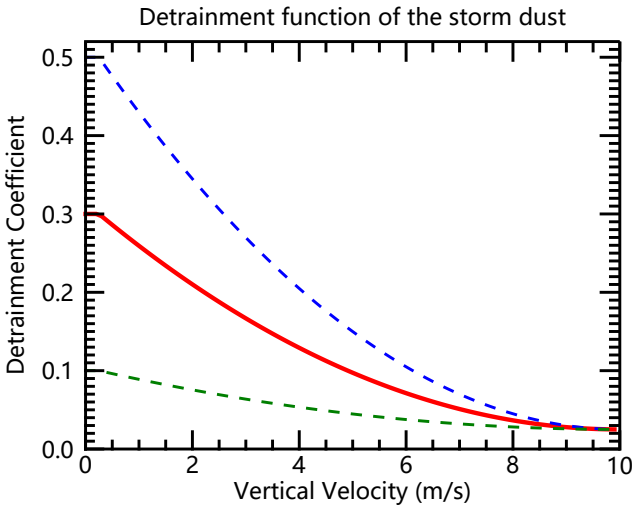

Figure 2: A quadratic function is used to describe the detrainment of the storm dust to the environment dust (see text). The coefficient of detrainment depends on the vertical velocity of the air parcel. The stronger the wind is, the weaker the detrainment is. In the parameterization, the maximum and minimum of detrainment coefficient is set to 30% and 2.5%, respectively (red line). The detrainment functions in the sensitivity studies for cases WD (green dash line, see the definitions of cases in Table 1) and SD (blue dash line) are also shown. The maxima of detrainment for case WD and SD are 10% and 50%, respectively.

of the storm dust in the nighttime.

2.4 Results

In this study, all the GCM simulations were performed at a spatial resolution of 64×48 grid points in longitude and latitude, and 29 vertical layers, reaching a maximum altitude of ∼80 km. The CDOD in the model follows the prescribed "Martian Year 29" (MY29 hereafter) dust scenario. The water cycle and photochemistry are turned off during the simulation in order to better diagnose the performance of the parameterization. Several parameters (see Table 1) in the parameterization needed to simulate rocket dust storms in the GCM are unconstrained and difficult to estimate. These include 1) the efficiency of the detrainment, 2) the reference mass mixing ratio used to estimate the size of the subgrid-scale rocket dust storm, and 3) the starting time and duration of dust injection.

2.4.1 Best-guess run

After exploring parameter space, we found the best match to mesoscale simulations of individual storms and overall vertical dust distributions observed by MCS was given by using the 'best-guess' parameters listed in Table 1. A simulation (case BG) with the these parameters is performed. Figure 3 displays the evolution of the storm case BG, occurring at longitude 84.5°W, latitude 56.25°N, around L_s = 153.8° in MY29, and the resulting detached dust layer. Before the onset of the rocket dust storm, no detached dust layers can be identified (Figure 3a). From LT 10:00 to 12:00, a rocket dust storm is triggered in the parameterization because the CDOD increases by ∼0.4 ($\Delta\tau_{dust}$). After the dust particles are lifted from the surface to the atmosphere, around LT 15:00 (Figure 3b), the rocket dust storm penetrates beyond the PBL, reaching an altitude of ∼18 km. Afterwards, the dusty air parcel (rocket dust storm) keeps rising until the disappearance of solar heating. At ∼LT

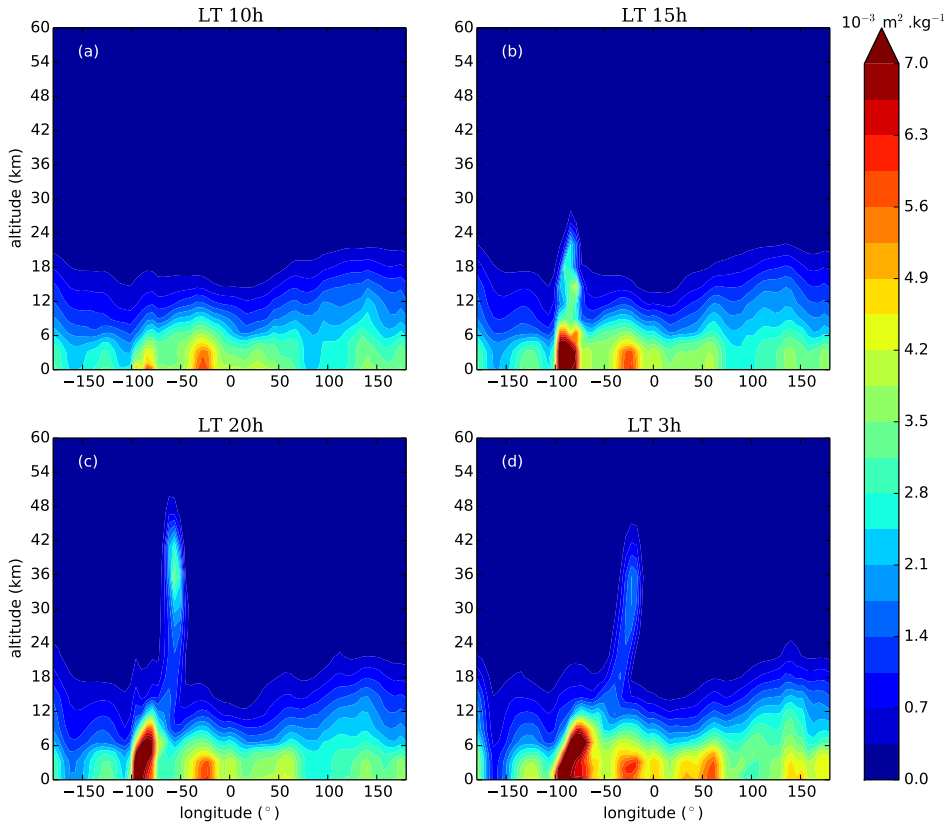

Figure 3: The best-guess case (case BG in Table 1) of a rocket dust storm. Cross-sections of the dust visible density-scaled opacity (DSO) at lat=56.25°N in (a) LT 10:00, (b) LT 15:00, and (c) LT 20:00 are shown. In (d), DSO at lat=52.5°N and LT 03:00 (on the next sol) is shown. Season is late northern summer (L_s = 153.8-154.4°).

20:00 (Figure 3c), the rocket dust storm reaches its highest altitude, ∼36 km. Not all of the storm dust is transferred to this altitude, because dust particles (storm dust) with low velocities are detrained to the environment dust as designed in the parameterization. After sunset, the storm dust sediments downwards owing to gravity and the negative buoyancy induced by the dust infrared cooling. At LT 03:00 on the next sol, the detached dust layer is still present at ∼30 km, as shown in Figure 3d. Because the detached dust layer moves equatorward, Figure 3d displays values at 52.5°N (not 56.25°N as in Figure 3a,b, and c). In this simulation, the detached dust layers peaks at ∼36 km. It is higher than the typical height that MCS observed, i.e. 20-25 km as introduced in section 2.1. This is reasonable because of two reasons: first, for an individual dust storm, the height it reached depends on its strength of convection. In this parameterization, a storm with higher $\Delta\tau_{dust}$ is expected to trigger deeper convection, thus a higher altitude it can reach. Therefore, the altitude an individual rocket dust storm reached is not necessary to be restricted at the range of the typical height of MCS observed detached dust layers. Second, the MCS observes Mars at two operating local time, i.e. 3:00 and 15:00. It is highly possible that MCS missed the moment when dust reached its highest altitude. Such as in this case, the storm reach ∼36 km at 20:00 local time. While at 3:00, it descended down by ∼6 km.

Table 1: Key parameter values used in the sensitivity studies

Name	max. of the detrainment	q_{ref}	t_{start}	t_{end}
BG (best-guess run)	0.3	5×10^{-4}	10:00	12:00
WD (weak detrainment)	0.1	5×10^{-4}	10:00	12:00
SD (strong detrainment)	0.5	5×10^{-4}	10:00	12:00
CS (clear storm)	0.3	2.5×10^{-4}	10:00	12:00
DS (dusty storm)	0.3	7.5×10^{-4}	10:00	12:00
EI (early injection)	0.3	5×10^{-4}	8:00	10:00
LI (late injection)	0.3	5×10^{-4}	12:00	14:00
LoI (long injection)	0.3	5×10^{-4}	10:00	14:00
SI (short injection)	0.3	5×10^{-4}	10:00	11:00

2.4.2 Sensitivity experiments

In order to determine the sensitivities of the parameters listed in Table 1, eight simulations with different values were performed. The setting of q_{ref} is related to the property of the initial rocket dust storm. The t_{start} and t_{end} are relevant to the lifting of dust particles. The detrainment function is associated with the interchange of storm dust and environment dust. Figures 4 and 5 summarize the evolutions of the rocket dust storm in the different simulations.

2.4.3 Detrainment

Among the parameters listed in Table 1, detrainment plays the most significant role in governing the evolution of the rocket dust storm. The functions of detrainment for the weak detrainment (WD) and strong detrainment (SD) cases can be found in Figure 2. The top of Figure 4 shows the same results as in Figure 3 (for best-guess case BG), but for WD and SD. As expected, the simulation with the weakest detrainment exhibits the deepest dust convection. The energy for supplying this motion is provided by the extra heating from the absorption of solar energy by the storm dust, controlled by the contrast of the amount of the dust in the environment and in the storm. The larger the contrast is, the larger the extra heating is (see Equation 5). With a strong detrainment, the storm dust is more efficiently supplied to the environment dust. For a weak detrainment, a larger $\Delta\mathcal{H}$ is expected and hence the rocket dust storm is capable of advecting to a higher altitude, as case WD shown in Figure 4. In the strong detrainment case (case SD), the rocket dust storm blows the dust particles up to $\sim$20 km in altitude, but no apparent detached dust layer forms. While in the WD case, the storm reaches $\sim$42 km in altitude at LT 20:00 and remains at $\sim$40 km by LT 03:00 the following sol. The height of the detached layer is higher by $\sim$6 km than in the best-guess simulation.

2.4.4 Strength of the initial storm

Because of the lack of information on each individual dust storm's spatial size, a reference mass mixing ratio needs to be assumed (see text in section 2.3.2). This value represents the dustiness of the rocket dust storm. A clearer (case CS) or dustier (case DS) storm will impact the estimation of the fraction of the storm. As a consequence, the contrast between the dust concentration of the environment and the storm will be changed. Varying the reference dust mass mixing ratio produces results similar to those produced by varying the detrainment strength by the same fractional amount, but with less variations in height and dustiness of the simulated dust layers. In the best-guess simulation, the storm extends to $\sim$36 km at LT 20:00. In case CS (Figure 4c3), a detached layer forms at $\sim$20 km. While by contrast, the dustier storm rises higher than 40 km at LT 20:00 in case DS.

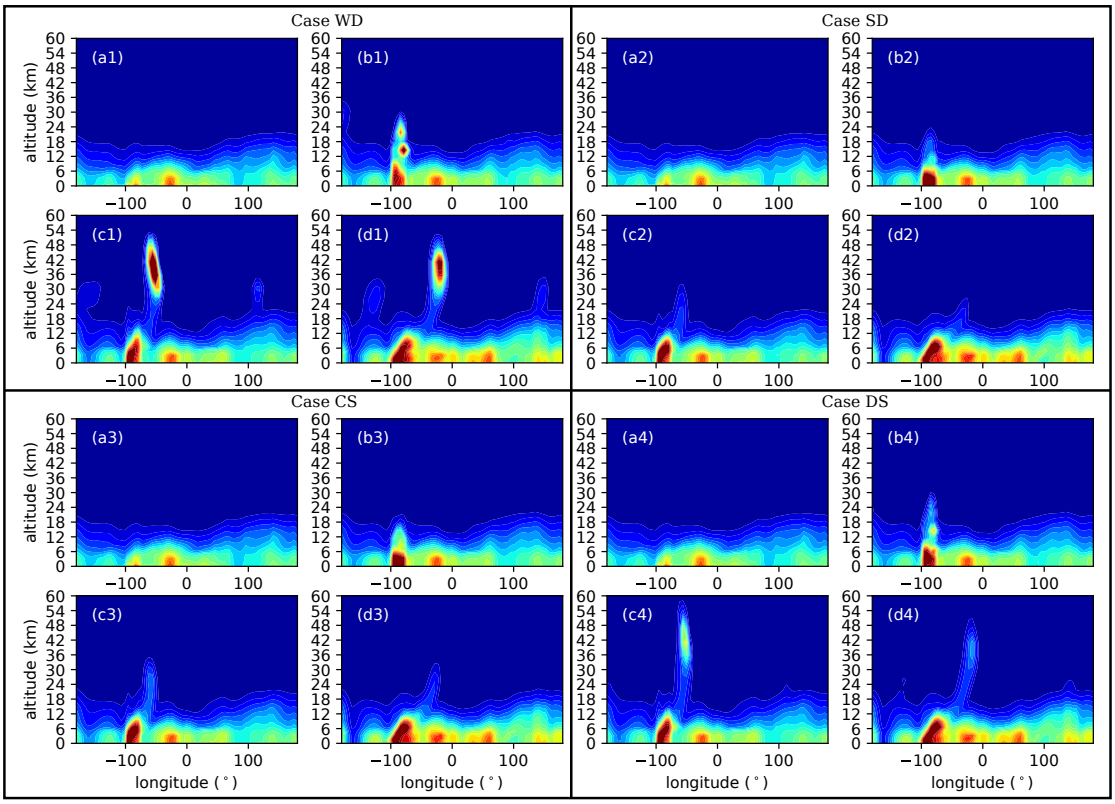

Figure 4: The cross-sections of dust DSO at the same time and location for comparison with the best-guess case in Figure 3, but from difference cases. The names of cases are labeled. The setting of parameters of different cases are list in Tab. 1. The data are plotted with the same colorbar in Figure 3. For each case, dust DSO at LT 10:00, 15:00, 20:00 and 3:00 are shown.

2.4.5 Dust injection timing

The extra heating provides buoyancy for supporting the rocket dust storm's ascent/descent. During the daytime, it is obvious that the earlier the dust particles are injected, the longer they are exposed to sunlight, hence the more solar energy they will absorb. As a result, the rocket dust storm can move upwards for a longer time. When the start time of dust injection is moved two hours earlier to LT 08:00 (case EI), but retaining the same total dust injection period of two hours, dust particles are transported to $\sim$42 km by LT 20:00 (Figure 5c5). This results in a higher detached dust layer than that in the best-guess case. Conversely, when the injection time is shifted two hours later (in case LI), this leads to less time exposure in the daytime, hence less energy for vertical motion. As a result, the detached dust layer forms at $\sim$20 km at LT 20:00 (Figure 5c6), lower than the one formed in the case BG.

Two simulations have been performed to test the sensitivity to the duration of dust lifting. For a given $\Delta\tau_{dust}$, the known amount of dust, estimated through Equation 2, can be injected to the atmosphere over a longer (four hours in case LoI) or shorter (one hour in case SI) time period. Compared to the best-guess simulation, fewer dust particles are lifted in each GCM timestep when the total injection period is longer. This leads to a less dusty air parcel. After the lifting, the difference in dust concentration between the rocket dust storm and the environment atmosphere is smaller than that in the best-guess case. Thus, following Equation 5, less heating will be provided for supporting the ascent of the rocket

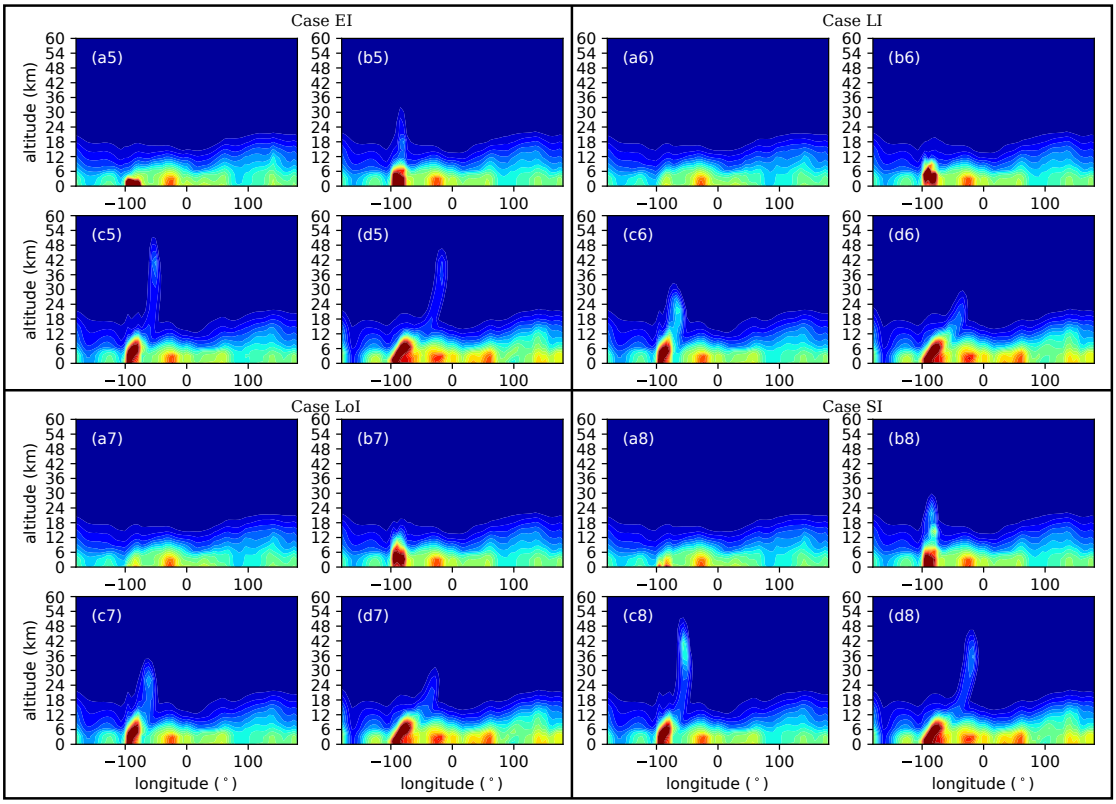

Figure 5: Same as Figure 4 except for cases EI, LI, LoI and SI.

dust storm. As shown in the Figure 5 a7-d7, the rocket dust storm mainly remains below 30 km. In the SI case, by contrast, a far dustier storm is created and more absorption of solar energy is expected. For case SI, deeper convection is shown in Figure 5 a8-d8, and storm dust is transported up to ∼40 km by LT 20:00.

2.5 Preliminary comparison with MCS observations

2.5.1 Simulation of a deep dust event

In order to validate the performance of the new parameterization, the model simulations are compared with MCS observations. To do this, an annual simulation of MY29 was run with the LMD Martian GCM with and without the parameterization. For the purpose of comparison between model outputs and satellite observations, the nighttime MCS data are used due to its better spatial coverage and precision compared to the daytime MCS data.

In MY29, around L_s = 145°, particularly opaque detached dust layers were observed by MCS in the northern hemisphere at latitudes around 30°N. The zonal mean dust DSO averaged from L_s = 143° to 147° is shown in Figure 6a. These detached dust layers appeared suddenly and were considered to be generated by a deep dust event by analyzing consecutive L_s bins for the MCS nighttime zonal averaged dust DSO from L_s = 130° to 165° [*McCleese et al.*, 2010]. After formation, the detached dust layers shifted equatorward and remained over the tropics after L_s = 155°. In the meantime, according to MARCI (the Mars Color Imager aboard MRO) observation reports, a sub-regional dust storm occurred at L_s = ∼144.4° and lingered over Eastern Chryse and West Arabia [*Malin et al.*, 2008]. The spatio-temporal information of this dust storm hints strongly that it is the source of the MCS-observed detached dust layer at L_s = 145°.

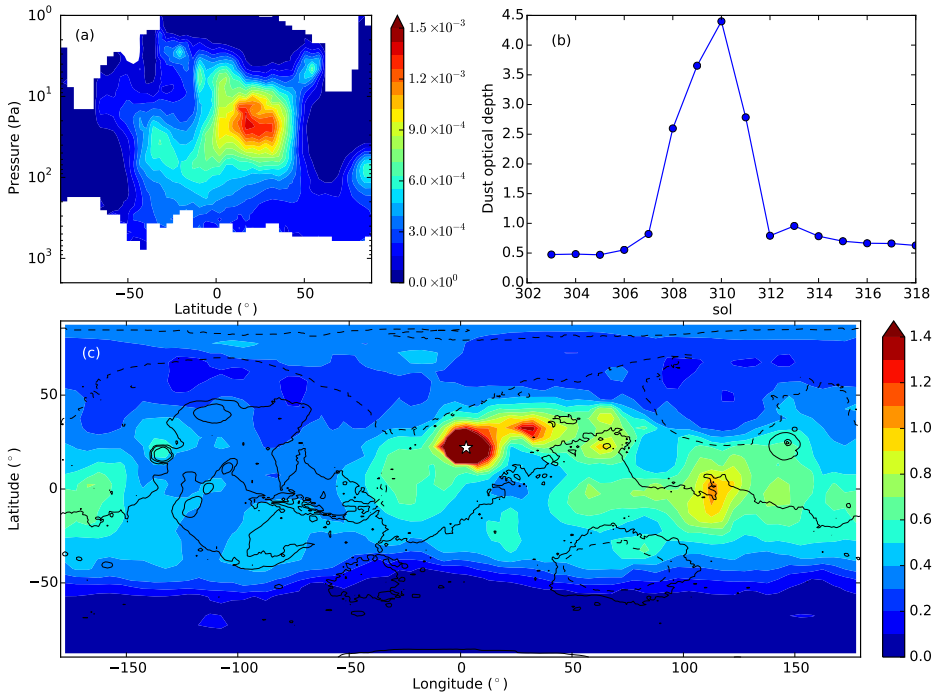

Figure 6: (a) The zonal mean of averaged MCS-observed dust DSO from L_s = 143° to 147°. (b) The evolution of column dust optical depth at the location labeled as white star in (c) the CDOD map at L_s = 146.0° in MY29.

In the MY29 prescribed dust scenario, the dust storm event observed by MARCI is included, as shown in Figure 6b and 6c. Figure 6c shows the global CDOD map at sol 310 of the MY29. A storm with an averaged dust optical depth larger than 2 is present. Figure 6b shows the temporal variation of dust optical depth at the center of the dust storm (marked as a white star in Figure 6c). The dust optical depth in the center first increases by > 0.2 per sol in sol 307, which is sufficient to trigger the rocket dust storm process in the GCM. Consequently, this event provides a clear-cut example to assess the impact of this deep dust storm event on the dust structures in the GCM, with our new rocket dust storm parameterization.

In Figure 7, the dust DSO distribution derived from the MCS observations is compared to simulations from the LMD Martian GCM with the rocket dust storm parameterization and from the traditional LMD Martian GCM (without the rocket dust storm parameterization). In Figure 7 a, c and e, the vertical variations in dust DSO from L_s = 135° to 175° are shown, while in Figure 7 b, d and f, the dust DSO averaged over longitude and time (from L_s = 145°-150°) are also displayed.

As can be seen in Figure 7a, before L_s = 145°, a thin detached dust layer is observed around 80 Pa. After L_s = 145°, the vertical dust distribution is significantly altered. The maximum of dust DSO is located at ∼30 Pa, and has been enriched by a factor of more than 2. Eventually, the detached dust layer moves downward and becomes fainter and fainter. Around L_s = 170°, the detached dust layer stops sedimenting at ∼150 Pa. Note that the DSO near the surface is very low, about 5 times lower than the maximum of the DSO along the vertical. While in Figure 7c, the dust, simulated by the traditional LMD Martian GCM (without the rocket dust storm parameterization), is mostly concentrated near the surface.

In the simulation including the rocket dust storm parameterization (Figure 7e), the dust vertical distribution has been dramatically impacted compared to the results from the traditional Martian GCM (Figure 7c and d). Between L_s ∼140°-150°, a detached dust layer is

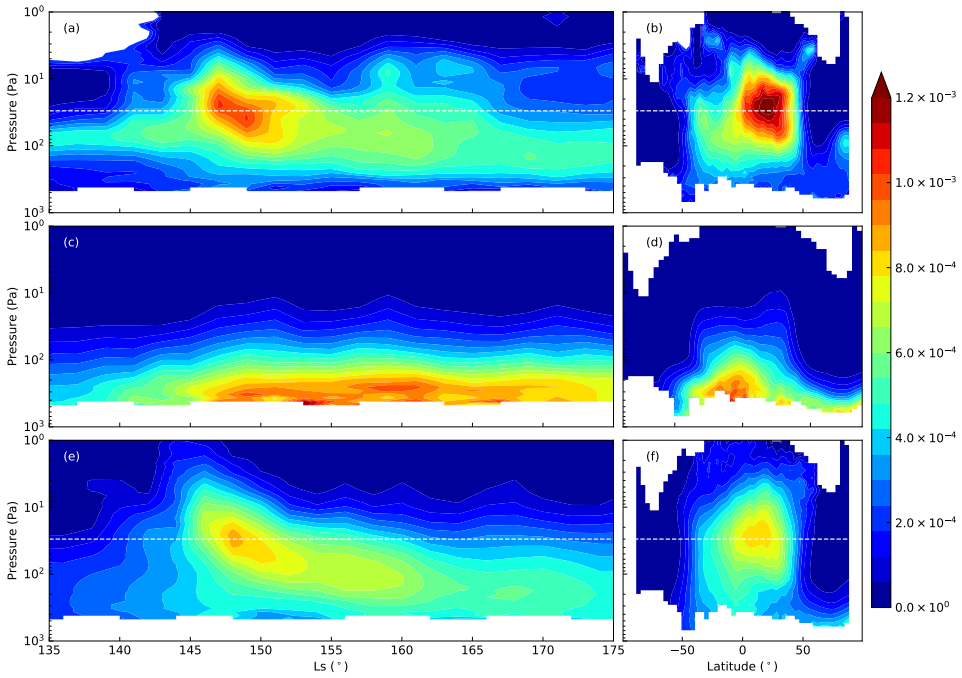

Figure 7: The nighttime dust DSO from the MCS observation (a, b), compared to simulations by our traditional GCM (c, d) and by the GCM with the rocket dust storm parameterization (e, f). All data are binned in L_s (every 5°). In the left column, the dust DSO is averaged over latitude from 25°S to 25°N and all longitudes are plotted. In the right column, the zonal mean of dust DSO from L_s = 145° to 150° are displayed. White dashed lines at a pressure of 30 Pa are plotted in the figure for better illustrating the altitude of the dust layers.

formed, at a height similar to the MCS observation (Figure 7a and b). After the formation of this detached dust layer, the dust starts to sediment. The dust evolution in this detached layer from the MCS observation and the GCM with the rocket dust storm parameterization are comparable until L_s ∼160°, although the simulated dust extends to slightly lower altitudes than the observed layer. In both cases, dust remained at a pressure level of ∼100 Pa (∼20 km). After that, a discrepancy in the dust vertical distribution becomes obvious. The dust observed by MCS tends to be stable at ∼100 Pa, whereas the dust simulated by the model keep sedimenting down to the Martian surface.

In Figure 7b, d and f, the dust DSO averaged over the whole longitudes and L_s = 145°-150° (which is corresponding to the dusty period in the Figure 7a) are shown. The observations retrieved by MCS reveal that the detached dust layer in Figure 7a is located in the northern hemisphere, from the equator to ∼40°N, whereas in Figure 7d, no detached dust layer can be identified above the PBL in the simulation using the traditional GCM. While in the simulation that includes the new parameterization(Figure 7f), a detached dust layer similar to that observed is produced. This dust layer is above the location where MARCI observed the reported dust storm [*Malin et al.*, 2008]. However, the GCM-derived peak DSO is lower than the MCS observation, i.e. in Figure 7a and b. The fact that the model does not completely reproduce detached dust layers may suggest that not all dust layers are induced by dust storm events.

The reported deep dust event is also simulated by the LMD Martian GCM with the rocket dust storm parameterization, but with different settings as described in Table 1. The simulated dust layers with the settings of cases WD, SD, CS and DS are shown in Figure 8. In Figure 8a and b, a higher and dustier dust layer compared to the one in Figure 7e and

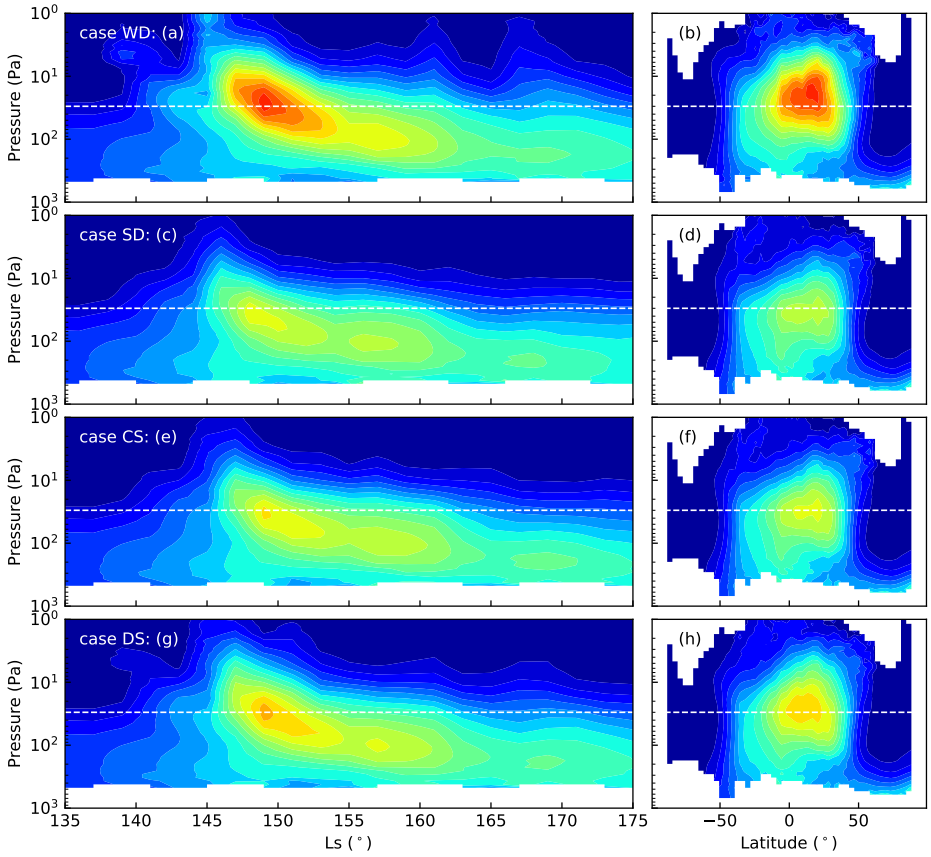

Figure 8: The nighttime dust DSO analogous to Figure 7 simulated by the GCM with rocket dust storm parameterization, but with the settings of cases WD, SD, CS and DS. The colorbar is not shown since it is the same to the one used in Figure 7.

f are produced with case WD setting. The dust concentration in this case are closer to the MCS observation (Figure 7a and b), but some extreme high dust layers are also simulated. A dust layer at a pressure of 1 Pa can be clearly seen in L_s = 145°. Another obvious dust layer at 5 Pa around L_s = 140° can be recognized. Detached dust layers in these heights are not seen in the MCS observation (Figure 7a and b). Therefore, a very weak detrainment is not recommended for the rocket dust storm parameterization. For the dust layer simulated with case SD setting, it is clearer and lower than the one shown in Figure 7e and f. Figure 8e, f, g and h show the simulated dust layers with settings of different reference dust mass mixing ratios (cases CS and DS). The height and concentration of the dust layer in Figure 8e and f (case CS) are slightly lower than the one in Figure 7e and f (case BG). The layer simulated with dusty storm setting (case DS), however, is similar to the one simulated with best-guess setting. This may be attributed to that this deep dust storm is very opaque that increasing its dustiness will not impact its energy balance significantly.

In Figure 9, the deep dust event is simulated with the settings of cases EI, LI, LoI and SI. In the simulation which dust is lifted over a long time period (case LoI), the dust concentration peaks at a lower altitude at L_s = ∼149° compared to the one simulated with best-guess setting. By contrast, at the same L_s, the dust DSO maximum appears at a higher altitude than the one in Figure 7e and f. Although the differences of the heights where the dust layers in cases BG, LoI and SI reached are subtle, the time period length of dust

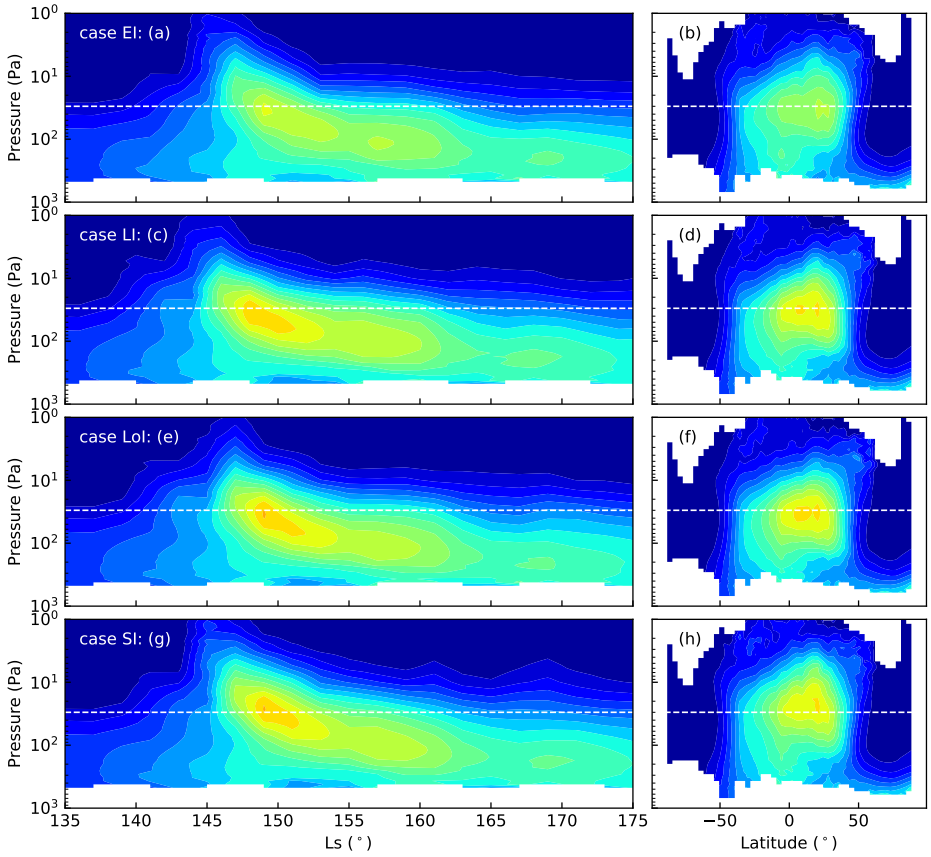

Figure 9: Same to Figure 8, but with the settings of cases EI, LI, Loi and SI.

injection functions a similar role as revealed in the sensitivity studies. In the sensitivity experiments, notwithstanding that earlier dust inject (case EI) results a higher detached dust layer, in this deep dust event simulation with case EI setting, a detached dust layer (Figure 9a and b) with comparable height to the one in Figure 7e and f (with case BG setting) is shown around $L_s = 150°$. But its dust concentration is lower than that in Figure 7e and f. In fact, the dust concentration difference in the simulations with cases BG and EI setting can also be found in the sensitivity experiments. The detached dust layer simulated with earlier dust injection (Figure 5d5) is clearer than the one in case BG (Figure 3d). It may be caused by that, earlier dust injection results in a longer stay for dust above the PBL, thus dust interacts with environment dust for a longer time (may also travels along with the horizontal jets). This will lead to the dilution of the storm dust. As a consequence, the low concentration of dust will lower the solar energy absorption. It plays a contrary role to long time exposure of dust in the daytime which will imply more absorption of solar energy. In fact, in the sensitivity experiment, the height of the detached dust layer formed in case EI in the sol after the rocket dust storm occurred is not higher than the one formed in case BG (Not shown in section 2.4, see their evolutions in the supporting information). Figure 9c and f show the detached structures of the deep dust event with setting of late dust injection (case LI). A lower detached dust layer is produce because of less solar energy absorbed.

By simulating the reported deep dust event with different set of the parameters, the comparison as shown in Figures 8 and 9 reveals similar results in sensitivity studies, where a individual rocket dust storm is simulated. The detrainment of storm dust to environment

dust impacts the formation of detached layers significantly. Meanwhile, varying dust contrast inside and outside of the storm and time period that the storm absorbs solar energy for can change the supply of convective energy, which will subsequently have an effect on the produce of the detached dust layers.

2.5.2 Annual simulation comparison

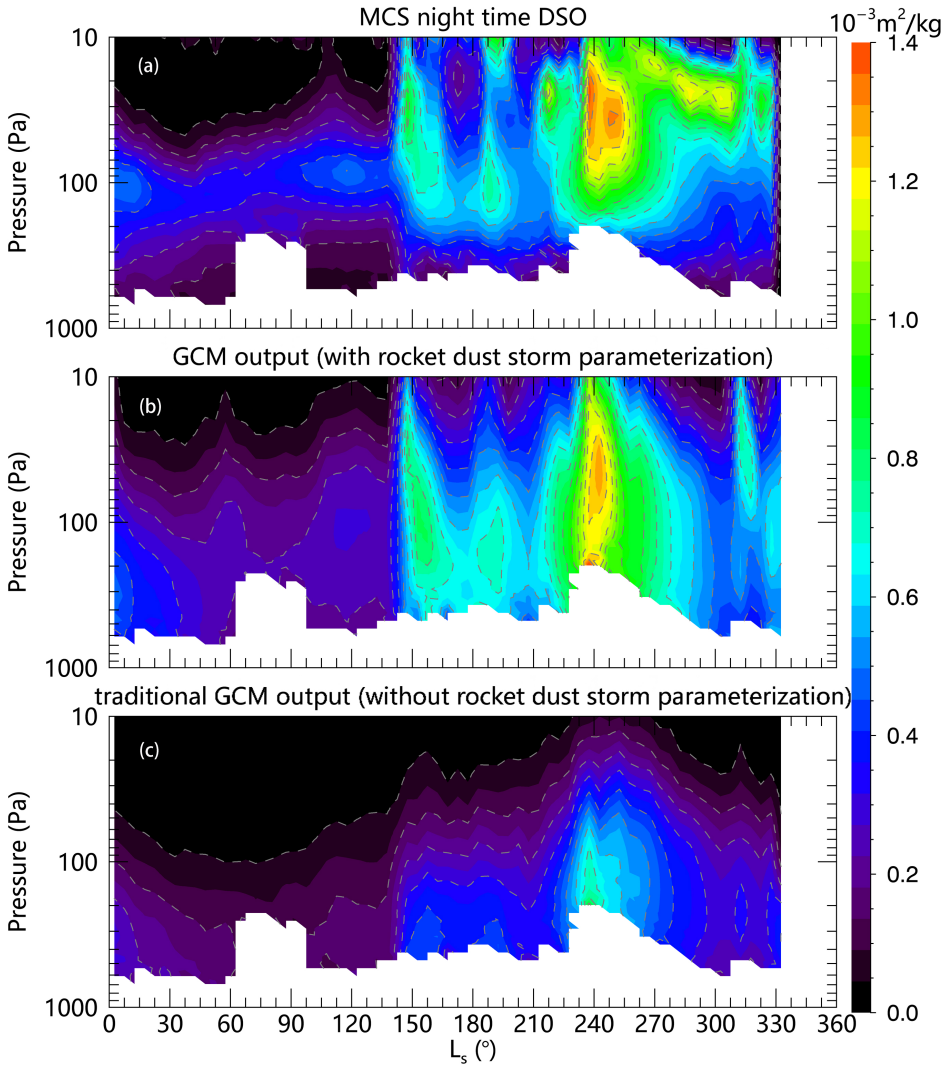

Figure 10: The temporal-vertical distribution of nighttime (LT 3:00) dust DSO over tropical regions (averaged over all longitudes and 10°N to 10°S) at infrared band (21.6 μm) at MY29 from (a) MCS observation, GCM output (b) with and (c) without the rocket dust storm parameterization are shown.

In Figure 10, the annual nighttime dust DSO vertical distribution over tropical regions during MY29 from the observations and from the GCM simulations (with and without the rocket dust storm parameterization) are shown. During the dusty seasons, the heights of the observed detached dust layers vary dramatically (Figure 10a), from 100 Pa to 10 Pa ($\sim$38 km). Compared to the observation (Figure 10a), the detached dust layers produced in the GCM (with the rocket dust storm parameterization, Figure 10b) are comparable to

the MCS-observed high-altitude detached layers. This implies that the vertical variation of the height of detached dust layers on Mars during the dusty season mostly originates from the deep dust storm events. However, the model simulation with the rocket dust storm process fails to account for the annual variations of the detached dust layers retrieved from the satellite observations, in particular, during the clear season. In Figure 10a, MCS data show that detached dust layers exist throughout the whole year. In the clear season, the detached dust layers' levels are quite stable, around 100 Pa. While, these features of the detached dust layers are not reproduced by the GCM including the rocket dust storm parameterization. The GCM produces detached dust layers in the late summer (around $L_s 120°$N). While the dust concentration is lower than that in Figure 10a. Meanwhile, no detached dust layers are produced at the beginning of the Martian year. The reason results in these failure may be that, in the GCM, during the clear seasons, the dust scenario does not report significant variations of dust optical depth. This leads to fewer local dust storms onsets in this season. As a consequence, no obvious detached dust layers form ($L_s < 150°$ in Figure 10b). This may hint that the observed detached dust layers in the clear seasons may be formed by processes other than rocket dust storms. Meanwhile, the detached dust layers after Ls $\sim$270° in Figure 10a also can not be explained by the rocket dust storms. These detached layers formed when fewer dust storms were reported (from MY29 dust scenario, dust activity starts to decrease after Ls $\sim$240°, see Figure 21 in *Montabone et al.* [2015]). And the heights of these dust layers are even higher than those layers simulated around Ls $\sim$240°, the dustiest time over MY29.

Another discrepancy between the simulation and the satellite observations is that, even if the rocket dust storms advect dust particles to high altitudes, the dust particles in the detached layers ultimately sediment onto the surface (similar to the dust distribution after $L_s > 160°$ in Figure 7e), resulting in the dissipation of the detached dust layers instead of remaining at a height of $\sim$20 km as seen by MCS.

These two inconsistencies may imply that the detached dust layers may also be generated by some other atmospheric processes, such as slope winds and/or scavenging of dust particles by water ice as discussed in the introduction section. A mesoscale diurnal slope circulation may be capable of providing continuous upward convection during the daytime, recycling dust particles into the atmosphere [*Rafkin et al.*, 2002]. *Navarro et al.* [2014b] report that in their GCM simulations, scavenging can not explain the formation of detached dust layers. No sufficient dust particles exist at the level where the water ice clouds are present. Another possibility for the inconsistencies between the model simulation and the observation could come from the missing observation of local rocket dust storms in the dust forcing scenarios. These dust scenarios are built based on the observations made by different Mars orbiting instruments. But if the rocket dust storm decays before or forms after the orbiter's operating local time, the instrument will be incapable of reporting the variation of dust concentration. The lack of rocket dust storms can also be explained by the trigger criterion in this parameterization (see text in section 2.3.1). Besides, the solar escalator mechanism plays a role in counteracting the dust sedimentation [*Daerden et al.*, 2015]. Dust motion analogous to the solar escalator can be seen in our simulations. But it is not strong enough to support the longterm sustenance of the detached dust layers. This may due to the poorly representation of solar escalator (possibly because of the coarse GCM resolution), or it may imply that the solar escalator is not the key factor to sustain the detached dust layers. Moreover, the performance of the parameterization may be limited by the its own ad hoc assumptions, such as the dust lifting scheme, the timing for dust injection and/or the reference mass mixing ratio for estimating the dust storm's scale. Further observations of mesoscale dust motion may be helpful to implement more realistic versions of this parameterization.

2.6 Conclusion on the rocket dust storm parametrization

In this paper, a rocket dust storm parameterization which is based on a parameterization of the dust transport by deep mesoscale convection during rocket dust storms, using global dust scenarios as a quantitative means to evaluate the occurrence of rocket dust storms, has been proposed and implemented in LMD Martian GCM. This implementation allows dust to be efficiently advected to high altitudes in the atmosphere. This was not possible in large-scale traditional Martian GCMs. Model simulations show that the dust cycle in the GCM including this parameterization can produce detached dust layers similar to the observed ones when intense storms are simulated. This suggests that the rocket dust storms are a key phenomenon to account for the detached dust layers on Mars. Nevertheless, there are inconsistencies between the simulation and observations. Further model developments, regarding the impact of local topographic circulations, and/or dust-water ice interactions, are needed to fully explore the origins of the detached dust layers on Mars. Meanwhile, more observations concerning local dust storms maybe helpful to refine this parameterization. Such as how the trigger of dust storm and dust lifting vary with local meteorological conditions, rather than with the dust scenarios in this study. Even the vertical velocities of the rocket dust storms are comparable to mesoscale simulations, studies with respect to dust mixing are still needed to detail the behavior of mesoscale dust convection. In addition, other strategies for parameterizing rocket dust storms in GCMs are also possible and might be proposed in future work, echoing the diversity of cumulus parameterizations in terrestrial GCMs.

3 Parametrization of detached dust layers triggered by slope winds

A further part of the work carried on the representation of the detached dust layers concerns their generation by slope winds. The parametrization of rocket dust storms presented in the previous section provides satisfying results in comparison to the observations during the dust storm period (Northern Hemisphere Winter). This confirms rocket dust storms are among key factors to explain the occurence of detached dust layers. However, the new parametrization fails to represent detached dust layers during the clear season, suggesting the involvement of other processes. Among them, which have already been mentioned in the previous section, the effect of updraft slope winds occuring during daytime and lifting the dust over high topography is considered. Indeed, a work initiated by Chao Wang has been carried on a parametrization of this process and is currently ongoing. The main principles of this parametrization are presented in this section.

3.1 Context

We assume a background atmosphere at rest with a temperature profile $T(z)$ (K), with z (m) the altitude above the surface.

Locally an atmospheric column is affected by local processes:

- A vertical updraft W_{up} at the bottom of the column, for instance due to convergent slope winds at the top of a mountain;
- A difference of temperature between the top of the mountain, at temperature T', and the free atmosphere besides, at temperature T;
- Enhanced dust loading inducing an additional extra radiative heating compared to the environment: $(\partial T \partial t)_{\text{rad}}$ (K s^{-1}).

As a result, the local column is characterized by a separate temperature profile $T'(z)$ and a local vertical wind profile $W(z)$ (m s^{-1}; > 0 when up) which can inject dust and other tracers in altitude.

We assume that we have a steady state. In the local column, $T'(z)$ and $W(z)$ are related by the following processes:

1. In steady state, the extra radiative heating at every altitude $H = (\partial T/\partial t)_{\text{rad}}$ is balanced by the adiabatic cooling:

$$W(\frac{g}{c_p} + \frac{\partial T'}{\partial z}) = H \tag{10}$$

   With g the acceleration of gravity (m s^{-2}) and c_p the specific heat at constant pressure (J kg^{-1} K^{-1}).

2. The acceleration of an air parcel is equal to the buoyancy forces (friction is neglected, as often in mass flux thermal parametrizations). In the lagrangian reference, this gives

$$\frac{DW}{dt} = g\frac{T' - T}{T}$$

   with the lagrangian derivative : $DW/dt = \partial W/\partial t + W\ \partial W/\partial z$. in steady state $\partial W/\partial t = 0$. therefore:

$$W\ \frac{\partial W}{\partial z} = g\frac{T' - T}{T} \tag{11}$$

3.2 Preliminary work: evaluation of the height hmons of subgrid mountains

As mentionned above, the model requires knowing the height of the local (subgrid) mountain present in the mesh. This height, $hmons$ is evaluated using the MOLA 8pixel/degree topography maps as follows:

1. Locate summits: On the MOLA topography, a 5x5 sliding window is used to search for summits. If the central pixel of the window is with the highest altitude, it is marked as a summit.
2. Locate the base of each summit:
   (a) obtain the "subarea" to look for the base: Expand the area around the summit in four directions. In each direction, stop expanding if (1) a pixel with an altitude which is higher than the summit is found, or (2) the distance between the summit and a pixel reaches 400 km (slightly larger than the radius of Olympus Mons).
   (b) search the base: In the "subarea", the distances from the summit to other pixels in the "subarea" are sorted incrementally and divided into intervals. For each interval, the averaged altitude is computed. Among these averaged altitudes, the smallest one is labeled as the altitude of the base.
   (c) The height of the mountain is the altitude difference between the summit and the base.
3. Resample to 1pixel/degree: For each grid cell (of 1 degree by 1 degree), the highest subgrid mountain from the higher resolution results is kept to represent subgrid topography.

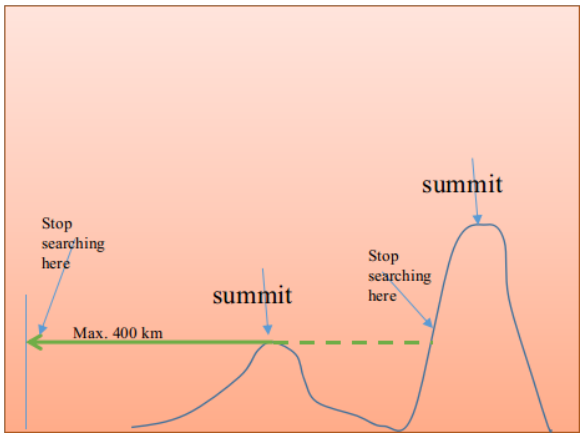

Figure 11: Schematic representation of the strategy used to evaluate $hmons$, the height of subgrid-scale mountains.

3.3 Discretization of the equations in the model

The modeled atmosphere consists of N layers with layer boundary values indexed X_l and X_{l+1} (with l numbered from $l = 1$ at surface to $l = N + 1$ at the top) and midlayer values indexed $X_{l+\frac{1}{2}}$.

Temperature are known in midlayers and the vertical wind are estimated at layer boundaries (to later compute vertical transport between layers).

1. Equation 10 can then be rewritten as:

$$W_l \, (\frac{g}{c_p} + \frac{T'_{l+\frac{1}{2}} - T'_{l-\frac{1}{2}}}{z_{l+\frac{1}{2}} - z_{l-\frac{1}{2}}}) = H_l \tag{12}$$

if H is previously at mid - layer like in the GCM, we use here:

$$H_l = \frac{1}{2}(H_{l-\frac{1}{2}} + H_{l+\frac{1}{2}})$$

2. Equation 11 can be written:

$$W_{l+\frac{1}{2}}(\frac{W_{l+1} - W_l}{z_{l+1} - z_l}) = g \, (\frac{T'_{l+\frac{1}{2}} - T_{l+\frac{1}{2}}}{T_{l+\frac{1}{2}}})$$

$$\frac{1}{2}(W_l + W_{l+1})(\frac{W_{l+1} - W_l}{z_{l+1} - z_l}) = g \, (\frac{T'_{l+\frac{1}{2}} - T_{l+\frac{1}{2}}}{T_{l+\frac{1}{2}}})$$

This yields:

$$W_{l+1}^2 - W_l^2 = 2g \, (z_{l+1} - z_l)(\frac{T'_{l+\frac{1}{2}}}{T_{l+\frac{1}{2}}} - 1) \tag{13}$$

Interestingly, the same discretized equation would be obtained by calculating the integrals in Equation 11 within each model layer if assumed to be isothermal (conservation of kinetic energy).

3.4 Description of the algorithm

- At the surface, we have $W_1 = 0$
- In the first layer we set $T'_{\frac{1}{2}} = T_{\frac{1}{2}}$
- At the top of the first layer, we prescribe the vertical wind induced by the mass convergence: $W_2 = W_{\text{up}}$ (This could be done elsewhere, for instance at the top of the boundary layer). We propose currently to prescribe a vertical wind W_{up} proportionnal to the buoyancy force and the height of the mountain $hmons$:

$$W_{up} = \alpha_{up} g \frac{T' - T}{T} hmons \tag{14}$$

The proportionnality coefficient α_{up} should represent the contribution of the friction along the slope, this part has to be further explored.

We then start a loop from $l = 2$ to $l = N$.

1. From equation 12, we can derive an estimation of the temperature in layer l of the column affected by the extra radiative heating and adiabatic cooling:

$$T'_{l+\frac{1}{2}} = T'_{l-\frac{1}{2}} + (\frac{H_l}{W_l} - \frac{g}{c_p})(z_{l+\frac{1}{2}} - z_{l-\frac{1}{2}}) \tag{15}$$

2. From this and equation 13, we can then estimate the vertical wind at the upper boundary of the layer, influenced by the buoyancy in the layer:

$$W_{l+1} = \sqrt{W_l^2 + 2g(z_{l+1} - z_l)(\frac{T'_{l+\frac{1}{2}}}{T_{l+\frac{1}{2}}} - 1)} \tag{16}$$

3. And we start again in the layer above.

A special case occurs if $(W_l^2 + 2g(z_{l+1} - z_l)(T'_{l+\frac{1}{2}}/T_{l+\frac{1}{2}} - 1)) < 0$.

This means that in layer l the vertical wind "overshoot" is stopped. More work could be done to understand this case, which may be an artifact.

In this case we then assume that the detrainment is such that the temperature in the column is equal to the background temperature, and that the vertical wind is set to the value that compensate the extra radiative heating by adiabatic cooling:

$$\text{if } W_l^2 + 2g(z_{l+1} - z_l)(\frac{T'_{l+\frac{1}{2}}}{T_{l+\frac{1}{2}}} - 1) < 0 \text{ then:}$$

$$T'_{l+\frac{1}{2}} = T_{l+\frac{1}{2}} \tag{17}$$

$$W_{l+1} = \frac{H_{l+1}}{(\frac{T_{l+\frac{3}{2}} - T_{l+\frac{1}{2}}}{z_{l+\frac{3}{2}} - z_{l+\frac{1}{2}}} + \frac{g}{c_p})} \tag{18}$$

The amount of dust lifted by this new scheme has also to be rescaled to the mesh area, as it only implies the part of the mesh occupied by the topography (the mountain doesn't occupy an entire mesh grid of the model as each mesh area is about 200kmx300km). Therefore we use an estimation of the fraction of the mesh concerned by the scheme of dust lifting by slope winds. Currently, we arbitrarily define this fraction, named $alpha$, as 10% of the relative topography of the mesh:

$$alpha = 0.1\frac{hmons - hmin}{hmax - hmin} \tag{19}$$

with $hmons$ the height of the higher topography within the cell, $hmin$, the minimal height of the topography over the whole planet, and $hmax$ the maximal height of the topography over the whole planet.

The transport and detrainment are then applied the same way as for the dust lifted by rocket dust storms (see previous section). The work described in this section has to complete the previous parametrization of the rocket dust storms, in order to fully reprsent the representation of detached dust layers. The life cycle of a dust detached layer formed by the process of convergent winds is depicted by FIGURE 12.

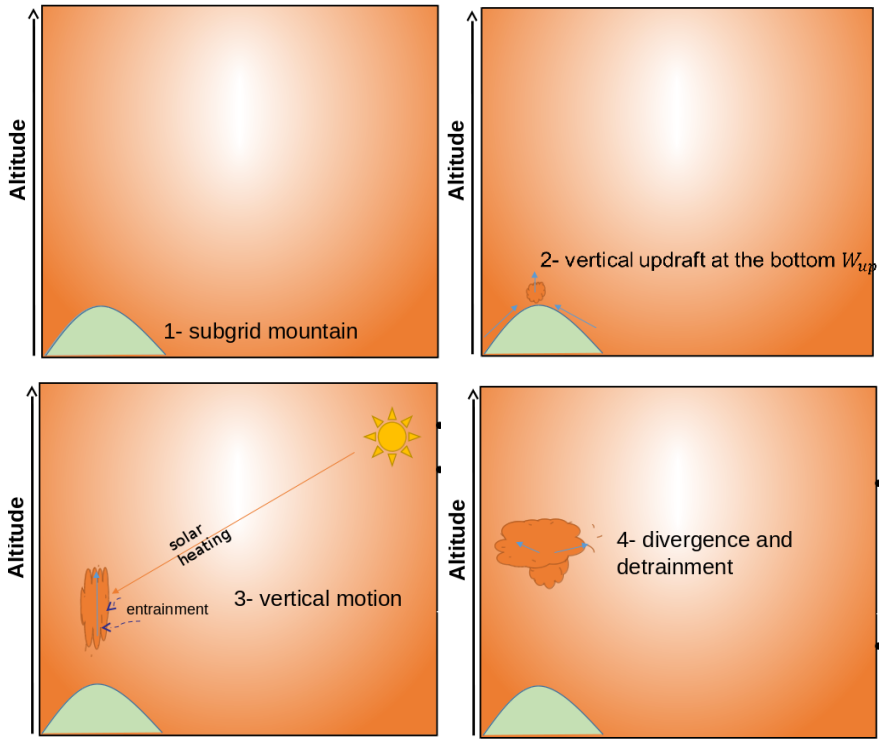

Figure 12: Figures representing the different steps, to be read from the left to the right, of the formation of a dust detached layer caused by slope winds over a mountain during daytime.

4 Investigating a new scheme of dust injection for the detached layer parametrization

4.1 Representation of dust in the GCM

In the LMD GCM, the radiative effect of an aerosol (particle of dust or water ice crystal) is computed assuming a log-normal size distribution characterized by the effective radius r_{eff} and effective variance ν_{eff} of the distribution. In practice these effective quantities correspond to the radius and variance weighed by the particle cross section.
The aerosols absorb and scatter solar and infrared radiations. The corresponding radiative transfer is characterized by spectral luminance, a source term and the cotribution from multiple scattering through the atmospheric layers. A key factor in the radiative transfer equation is the (non-dimentional) optical depth, which is a function of the particle amount and their spectral extinction cross-section (the later being the sum of absorbtion and diffusion cross-sections). A more convinient related parameter is the efficiency factor Q_{ext} which is the ratio between the spectral extinction cross-section and the geometric projection of the parrticles. In the GCM, aerosols are caracterized by theeir mass mixing ratio q, i.e. the mass of aerosols per unit of mass of the atmosphere, and their size distribution given by r_{eff} and ν_{eff}. The optical depth of each atmospheric layer is given by :

$$\tau_\lambda = \frac{3}{4} \frac{Q_{ext_\lambda}\, q}{\rho_{dust}\, r_{eff}\, g}\, dp \tag{20}$$

where τ_λ is the spectral optical depth, Q_{ext_λ} the spectral efficiency factor, q the dust mass mixing ratio (in kg of dust per kg of air), ρ_{dust} the density of dust (in kg.m$^-$3), r_{eff} the effective radius of the particule distribution (in m), g is gravity (in m.s^{-2}) and *dp* is the pressure difference (in Pa) between bottom and top of the atmospheric layer.

4.2 Goal of the new dust injection scheme

The goal is here to test an improvement of the current dust prescription setup in the GCM, where observed dust opacities ([*Montabone et al.*, 2015]) are imposed: At every time step dust is injected at the base of the atmosphere, and also freely transported (vertically and horizontally) in the model, but it is systematically rescaled so that the column opacity matches the prescribed dust scenario. This unphysical normalization is a way to ensure that the modeled dust cycle matches the observed one.
An obvious way to improve this strong normalizing procedure is to find a procedure where dust is adequately injected (and still freely transported) in the model. The difficulty is then to devise a scheme which, based on the target obseved opacities, will indeed produce the sought dust cycle.
For this preliminary study, various injection procedures have been investigated :

- instanteneous injection of dust at the base of the atmosphere,
- injection of dust at the base of the atmosphere spread over a third of the day (i.e. from late morning to evening; when the planetary boundary is active and dust lifting favored),
- injection of dust in altitude around 10 or 30 km, in order to represent the effect of sub-grid scale turbulence and localized transport (e.g. due to rocket dust storms) that would redistribute injected dust at high altitudes.

4.3 Instanteneous dust lifting at the base of the atmosphere

4.3.1 Modifying the amount of dust in the atmosphere

In practice, at the first time step the model will load the reference value $\tau_{ref\ scenario}$ of the dust opacity provided by the dust scenario. From this reference value, the following steps are followed :

- the mixing ratio of dust in each layer and for all locations on the planet is computed,
- these mixing ratios are used to compute the radiative transfer,
- the optical depth of each layer is computed,
- the total column opacities τ_{ref} (normalized to 610 Pa, the same reference value than for the provided dust scenarios) are computed and compared to $\tau_{ref\ scenario}$

To model a dust injection corresponding to the difference $d\tau$ in column opacities between $\tau_{ref\ scenario}$ and τ_{ref}, a specific module has been designed. The resulting increment is however only applied on a physical basis and thus :

- only positive values of $d\tau$ are allowed: this is to enforce that only addition of dust is done by the scheme. In practice negative values of $d\tau$ correspond to an excess of dust (compared to the scenario value) which will be depleated by physical processes such as sedimentation and advection.
- Increments of dust are only applied during the daytime (local true solar time between 10h and 18h) to account for the fact that dust lifting and mixing into the atmosphere is related to planetary boundary layer processes.
- There can be no increment of dust when there is CO2 ice present on the surface below, as there is no available dust to be lifted (since it is trapped in the CO2 ice).

$d\tau$ is provided as an input to the vertical turbulent diffusion routine which computes the vertical turbulent diffusion from the surface layer to the rest of the atmosphere using equation 4.3.1 to determine the amount of dust that needs be added to the firts layer :

$$dq = \frac{4}{3} \frac{p_{surf}}{p_{ref}} \frac{\rho_{dust}\, r_{eff}}{Q_{ext}\, \Delta t}\, d\tau \tag{21}$$

Where *dq* is the change in mixing ratio of dust (kg/kg$_{air}$), p_{surf} the surface pressure (Pa), ρ_{dust} the density of dust (kg.m$-$3), r_{eff} (m) the effective radius of the dust particle distribution, p_{ref} a reference pressure (610 Pa), Q_{ext} the efficiency factor, Δt (s) the duration over which the injection is done and $d\tau$ the column opacity difference between the GCM and the dust scenario.

4.3.2 Results with instantaneous injection at the surface

During Mars Year 29, as in other years, many local and regional dust storms were observed. For this study, we have focused on a specific one which occured around Ls=143.4°at longitude 0° E, latitude 22.5° N (FIGURE 13). To evaluate results, we follow the evolution of

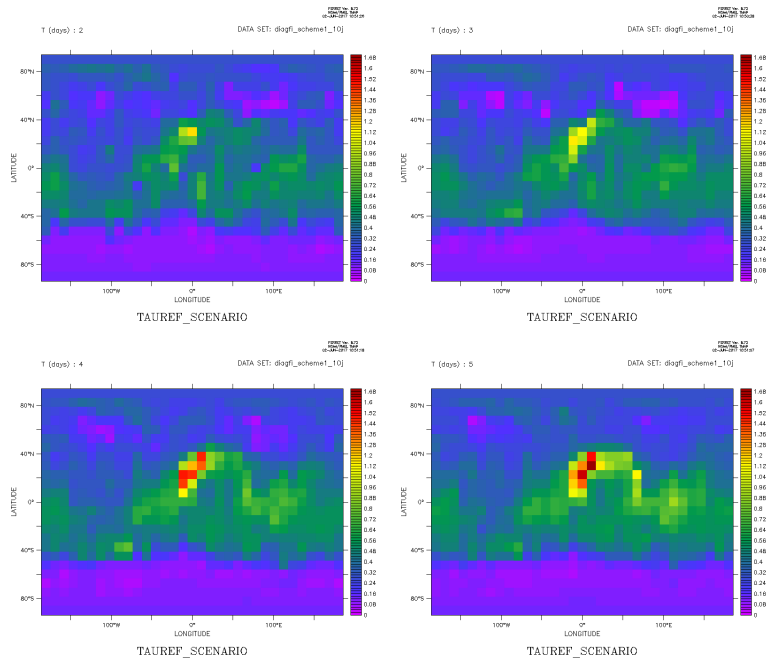

Figure 13: Maps of daily reference column optical depth from the MY29 dust scenario, at solar longitude Ls=143.39° ; for sols 2, 3, 4 and 5 of a ten sol long simulation. At the grid point located at 22.5° N, 0° E, the increase of opacity reveals the emergence of a local dust storm.

$\tau_{ref\ scenario}$ and τ_{ref}, at 22.5° N, 0° E over a duration of 10 sol starting at Ls=143.39°(see FIGURE 14). Note that in the original scheme, dust is normalized at all time and location to exactly match the reference opacity $\tau_{ref\ scenario}$. FIGURE 14 shows that during the first steps through the day (before 10h) τ_{ref} is well below $\tau_{ref\ scenario}$ which evolves from 0.7 to 0.8. However, as soon as the local time reaches 10h (i.e. 0.438 fraction of a sol), dust injection occurs and the value of τ_{ref} overshoots that of $\tau_{ref\ scenario}$ by around 0.022. Once above the reference value the injection scheme is (by design) off and there is thus no further dust injection during that day. τ_{ref} then oscillates between 0.8 and 1 during the end of day and night and reaches a value close to $\tau_{ref\ scenario}$ the next morning. During sol 1 no injection occurs because τ_{ref} is higher than $\tau_{ref\ scenario}$. Only sedimentation (and hrizonatl advection) acts to decrease the local opacity. At sol 1.958 τ_{ref} becomes lower than $\tau_{ref\ scenario}$, thus injection occurs as soon as the local time permits it, i.e. at time 2.438, where τ_{ref} increases from 0.704 to 1.255 and catches up with $\tau_{ref\ scenario}$ which is then 1.259. This pattern of injection occurs over the following 6 sols. At sol 7 and beyond, τ_{ref} is always greater than $\tau_{ref\ scenario}$ and there is no more injection. It is worth noting that the computed opacity has a strong diurnal cycle, regardeless of injections.
This preliminary study shows that with brief and strong injections it is feasible to force the GCM to overall follow a prescribed dust sceanario. It however is also clear that forcing an instantaneous injection (i.e. over a single physics time step of 15mn) of dust is not very realistic and that the injection might be more gradual and more likely should be spread over

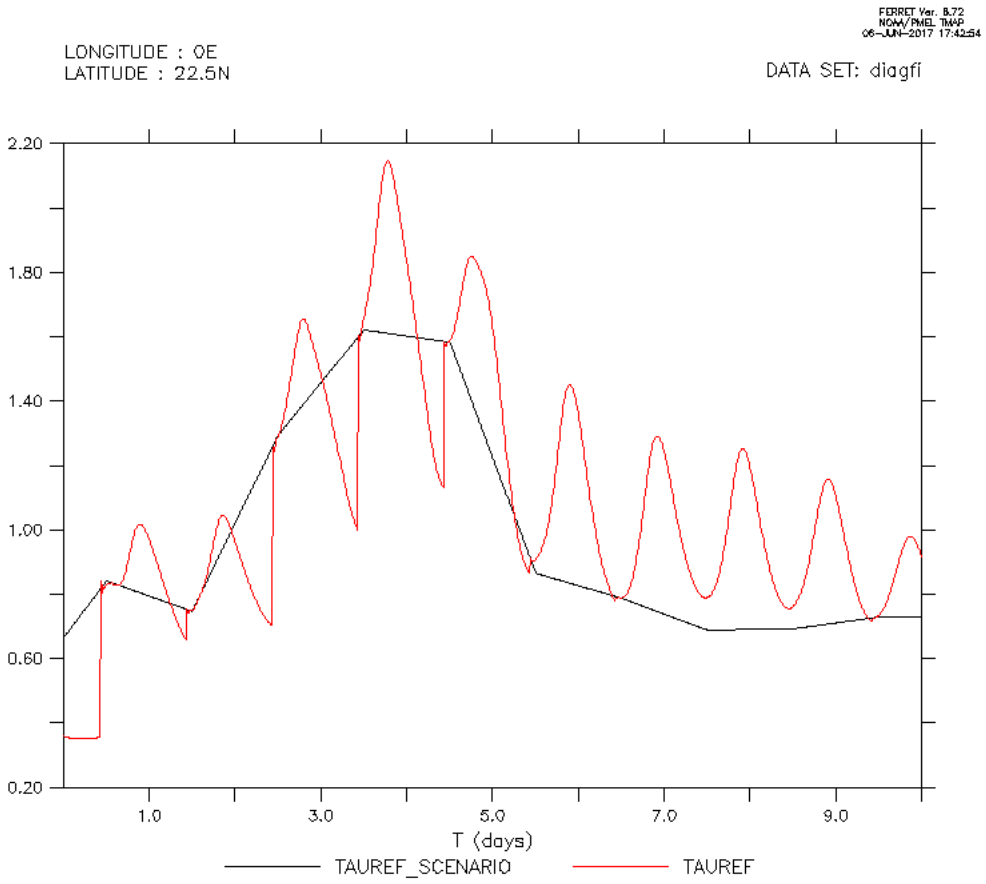

Figure 14: Evolution of τ_{ref} and $\tau_{ref\ scenario}$ (normalized to a reference surface pressure of 610Pa) over 10 sols, starting at Ls=143.39°, using the MY29 dust scenario. The dust scenario value (1 value per sol in the datafile, linearly interpolated over time) is in black, and the dust obtained in the GCM when injecting dust at the surface enabled only between 10h and 18h is in red. Note the oscillations of τ_{ref} depicting a strong diurnal cycle of atmospheric dust.

a longer duration, which is described in the following section.

4.4 Dust lifting over the daytime at the base of the atmosphere

4.4.1 Modeling an injection from 10h to 18h

As shown above, it makes sense to spread the injection of dust over a time span rather than asume it occurs instantaneously. In practice values from the dust scenarios are given once per sol, mostly from observations in the early afternoon. The choice here is then to use this target value assumed to be valid at 14h, but spread the added injection over the daytime interval of 10h to 18h, when the planetary boundary layer is active.

4.4.2 Results with continuous daytime injection at the surface

FIGURE 15 displays the same fields (again, at location 22.5°N, 0°E) as in FIGURE 14 using the scheme described above. Over the first few steps of the simulation the same evolution of τ_{ref} is obtained as no injection occurs. At time 0.594, i.e. 14h local time, the value of $\tau_{ref\ scenario}$ is read from the dust scenario and triggers the dust injection scheme as it is higher than τ_{ref} at the same time. However the injection is spread over the rest of the day, until 0.75 (18h, local time). There is then no injection until the following morning at 10h, at time 1.417 where injection resumes. The injection continues until time 1.656 when it is 14h and a new value of $\tau_{ref\ scenario}$ is loaded. At that time τ_{ref} is lower than $\tau_{ref\ scenario}$ so a new injection rate is computed and used until time 1.75 (18h local time), set to zero during the night and resumed the next morning at 10h. This continues over the next four days where at 14h the computed value of τ_{ref} is systematically lower than $\tau_{ref\ scenario}$. During the fifth day, τ_{ref} is larger then $\tau_{ref\ scenario}$ and thus no injection is triggered. This is the case over the last few days of the simulation.

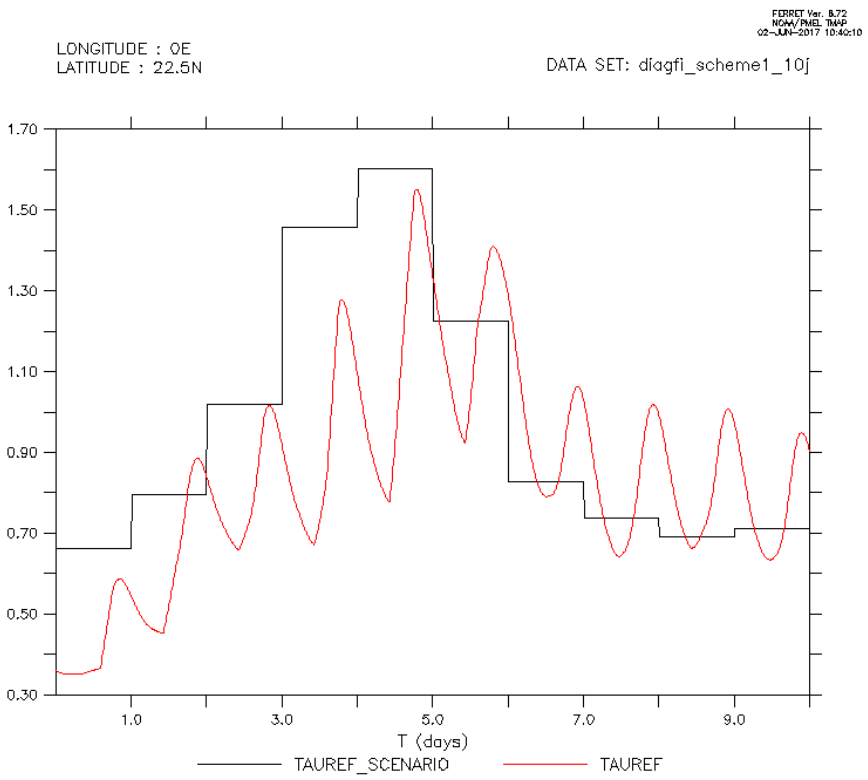

Figure 15: Evolution of τ_{ref} and $\tau_{ref\ scenario}$ (normalized to a reference surface pressure of 610Pa) over 10 sols, starting at Ls=143.39°, using the MY29 dust scenario. The dust scenario value (1 value per sol in the datafile, assumed valid at 14h) is in black, and the dust obtained in the GCM when injecting dust at the surface over the daytime (from 10h to 18h) is in red. Note the oscillations of τ_{ref} depicting a strong diurnal cycle of atmospheric dust.

4.4.3 Stability of the dust injection scheme over a year

A year-long simulation was run to study the long term evolution of dust opacity and evaluat e the stability of the dust injection scheme. Results are given in FIGURE 16.

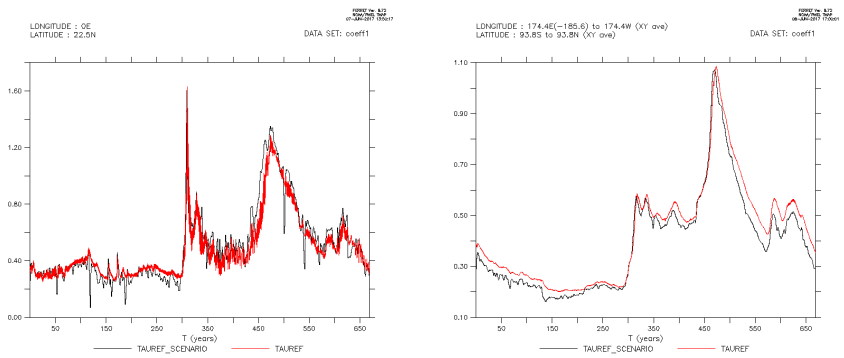

Figure 16: Evolution of τ_{ref} and $\tau_{ref\ scenario}$ over a Martian year at a reference location (22.5°N, 0°E) (left plot) and averaged over the planet (right plot), using the MY29 dust scenario. The dust scenario opacity $\tau_{ref\ scenario}$ is displayed in black and the computed GCM dust opacity τ_{ref} when injection is done at the surface over the daytime (from 10h to 18h) is displayed in red.

These plots show that overall the GCM opacity follows the general trends from the dust scenario. The opacity anomaly (difference between scenario and GCM values) is given in FIGURE 17. In the equatorial regions the opacity computed by the GCM is quite close to the values in the scenario during the whole year. Larger differences arise in the polar reagions. In the second half of the year there is much more dust in the northern polar region in the GCM. This may be due to the fact that dust advected there should be scavenged by CO_2 clouds which are not represented in the model. The lack of dust obtained by the GCM in the southern polar region during the second half of the year (i.e. starting with the Southern Hemisphere spring) may be due to the imposed limitation in the scheme of canceling any dust injection when there is some CO_2 ice on the surface in the GCM mesh. In reality the local CO_2 coverage is more patchy and the strong local surface differences (between snow covered and snow free areas) liquely generate strong thermal breeze which would lift dust. Many local dust storms are indeed observed (e.g. FIGURE 18) at this location and time of year.

At this point the injection scheme has only focused on injecting dust at the surface, assuming that the relevent physical parametrizations would handle the vertical transport of dust (e.g. to generate dust detached layers). In the following sections, we test injecting dust directly in altitude, in order to evaluate if results then better match observations.

4.5 Injecting dust in the planetary boundary layer and above

In this section we test injecting dust at different altitudes (a coarse representation mimicking sub-grid scale processes such as rocket dust storm). Firstly by assuming that the planetary boundary layer very actively mixes the added dust (and thus adding it over the first 10 km of the atmosphere), and secondly by adding the dust at 30km, the altitude at which detached dust are typically observed. This last case enables evaluating if dust, once brought to these altitudes, would indeed spread there as a detached dust layer. In both cases, the injection of dust is done with the same rules as developped in the previous section (i.e. injection will be triggered if computed opacity are lower than the scenario opacities at 14h, and injection will be spread over the daytime, from 10h to 18h).

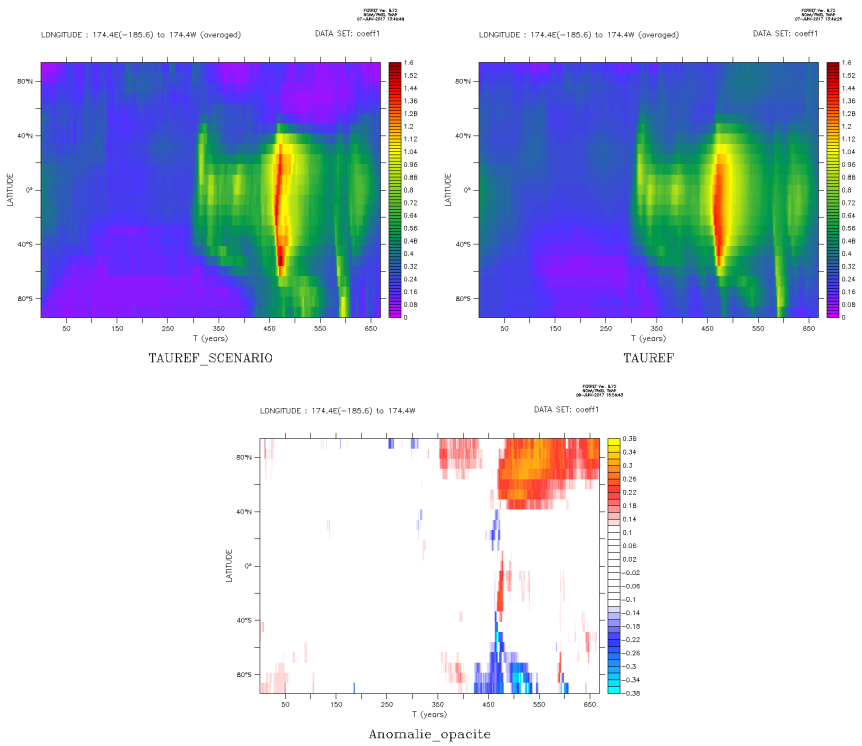

Figure 17: Zonally averaged opacity over the Martian year: observed $\tau_{ref\ scenario}$(left), computed by the GCM τ_{ref}(right) and anomaly (bottom) $\tau_{ref} - \tau_{ref\ scenario}$.

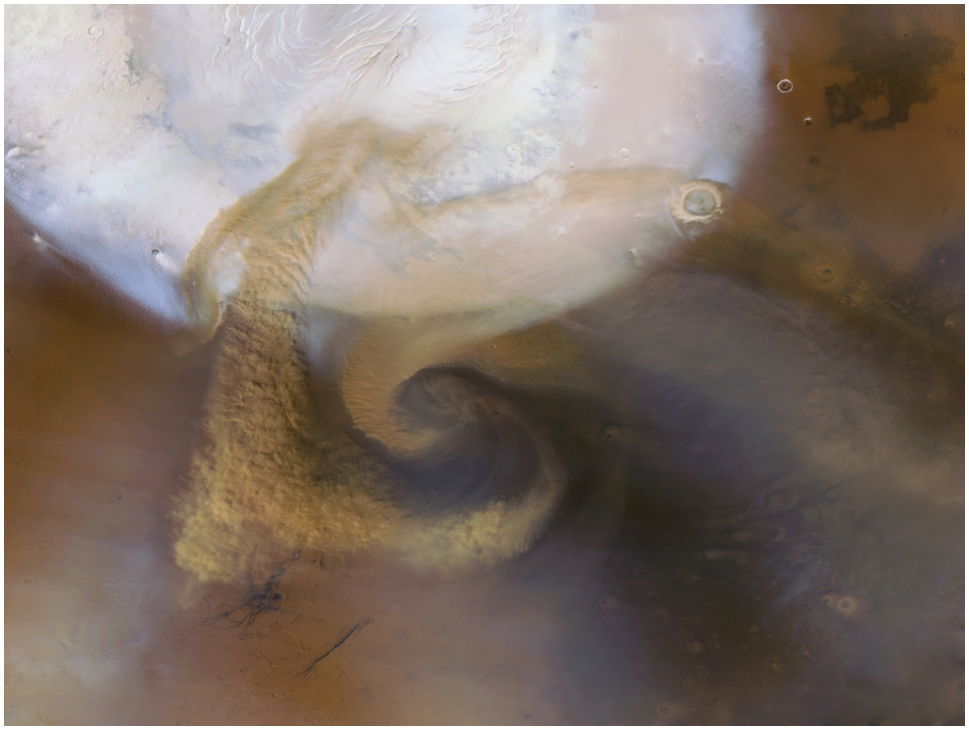

Figure 18: Image of a local dust storm in the Southern polar region of Mars during Southern polar spring. The local temperature gradient due to the combined presence of cold CO_2 ice on the surface and warmer ice-free surfaces generates a thermal breeze which, combined to the Coriolis force, leads to a rising swirl of dust.

4.5.1 Injecting dust over the first 10 km of altitude

A local dust lifting event is essentially a sub-grid process when compared to the typical size of the GCM mesh. If the turbulence is intense then one may assume that the lifted dust is instantaneously mixed within the planetary boundary layer at the spatial scale resolved by the model. Thus the dust injection may simply be done over the first 10km of the atmosphere rather than at the surface. In terms of the injection scheme, this implies that the amount of injected dust $d\tau$ will be injected over layers 1 to n, where n is the atmospheric layer at altitude 10km, as :

$$dq_l = \frac{4}{3} \frac{r_{eff}\ \rho_{dust}}{Q_{ext}} \frac{p_{surf}}{p_{ref}} \frac{d\tau}{(t_e - t_s)\ 88775} \frac{g}{\Delta p_l} \tag{22}$$

where t_e and t_s are respectively the ending and starting times (in fractions of sol), p_{ref} the reference surface pressure (610 Pa), 88775 the number of seconds in a Martian sol and Δp_l the pressure difference (in Pa) between the bottom and top of the l-th atmospheric layer. In practice dq_l is directly and homogeneously added to the dust mixing ratios in the model, without any injection at the surface relayed by the vertical turbulent mixing module.

4.5.2 Injecting dust up to 30km of altitude

As mentionned previously, the goal here is to assume that local unresolved transport phenomenas (e.g. rocket dust storms) are able to transport dust up to 30km (i.e. above the boundary layer). In practice this simply means using equation 22 but extending it up to the atmosphic layer n 30km above the surface.

4.5.3 Results of the injection schemes

In this section, results are shown and compared for the following three injection schemes:

- Scheme 1: the surface injection scheme
- Scheme 2: homogeneous dust injection over the first 10km of altitude
- Scheme 3: homogeneous dust injection over the first 30km of altitude

Results are shown in FIGURE 19 at the reference location (22.5°N, 0°E). As can be seen in the figure on the first day injection starts at the same time, i.e. 14h, once a reference $\tau_{ref\ scenario}$ is read. However the dust increment over 10 or 30 km (schemes 2 and 3) clearly generates larger opacities (1.979 for scheme 2 and 1.620 for scheme 3 at time 1.917) than the surface injection scheme. Because of the added dust for schemes 2 and 3, there is no injection needed on the following day. On the third day, values of τ_{ref} become smaller than $\tau_{ref\ scenario}$ and more injections are triggered. On the third day at 14h, conditions to trigger injection are again reached. Overall maximal opacities of 2.872 at time 4.74 and 2.027 at time 4.594 are respectively reached for schemes 2 and 3. This shows that schemes injecting dust directly in the atmosphere generate higher opacities than observed; inpratice by a factor 1.8 for scheme 2 and 1.3 for scheme 3. Both schemes 2 and 3 seem "too efficient", and scheme 3 lies in most cases closer to the target values.

What is said above is focused on the column opacity values, but another key parameter is the resulting vertical distribution dust. Profiles of dust mixing ratios at chosen time during the simulation are shown in FIGURE 20. FIGURES 20a and 20b display profiles for the different injection schemes before and after the injection step. These figures illustrate that the altitude locatization of dust injection has little impact on the overall vertical profile of dust. FIGURES 20c and 20d display profile at the thrid and ninth sol of the simulation. A dust detached layer can be seen to emarge around 30km for scheme 3 on the third sol of the simulation and is still present on the ninth sol of the simulation. This implies that once the

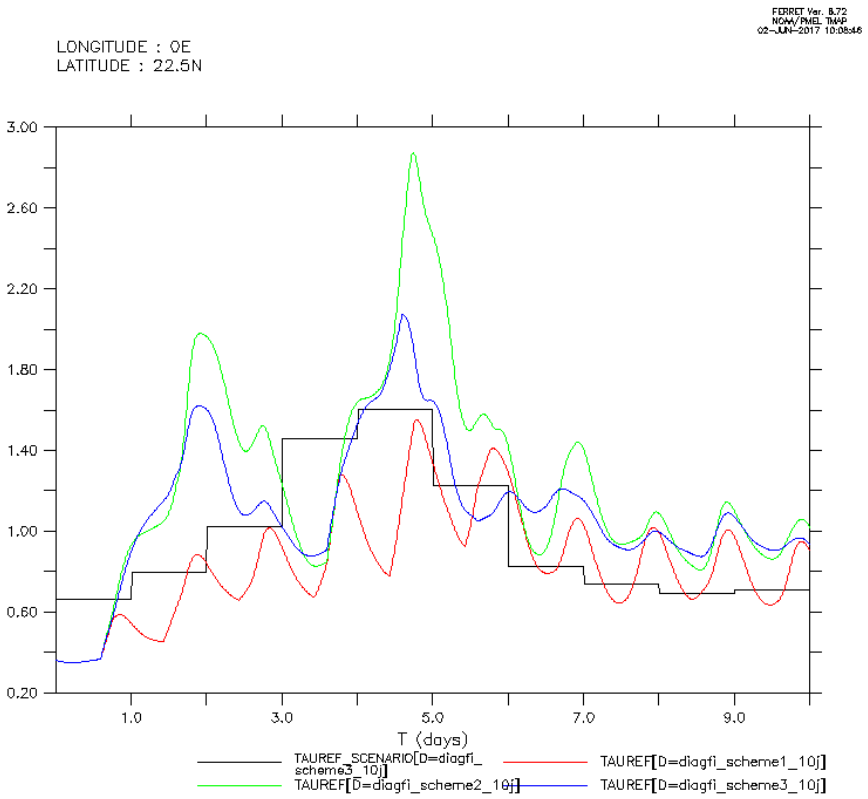

Figure 19: Evolution of the optical depth using various injection schemes, for a 10 sol-long simulation starting at Ls=143.39°, using the MY29 dust scenario. Black line: the reference optical depth from the MY29 dust scenario (1 value per sol, assumed valid at 14h). Red line: the optical depth computed using the daytime surface injection scheme. Green line: the optical depth computed using the dust injection scheme over the first 10km of altitude. Blue line: the optical depth computed using the dust injection scheme over the first 30km of altitude.

dust has reached these altitudes it is maintained there through large scale processes. With scheme 2, a detached dust layer around 30km also eventually arises, also showing that large scale processes, once dust is sufficiently aloft, are capable of generating and maintaining detached dust layers.

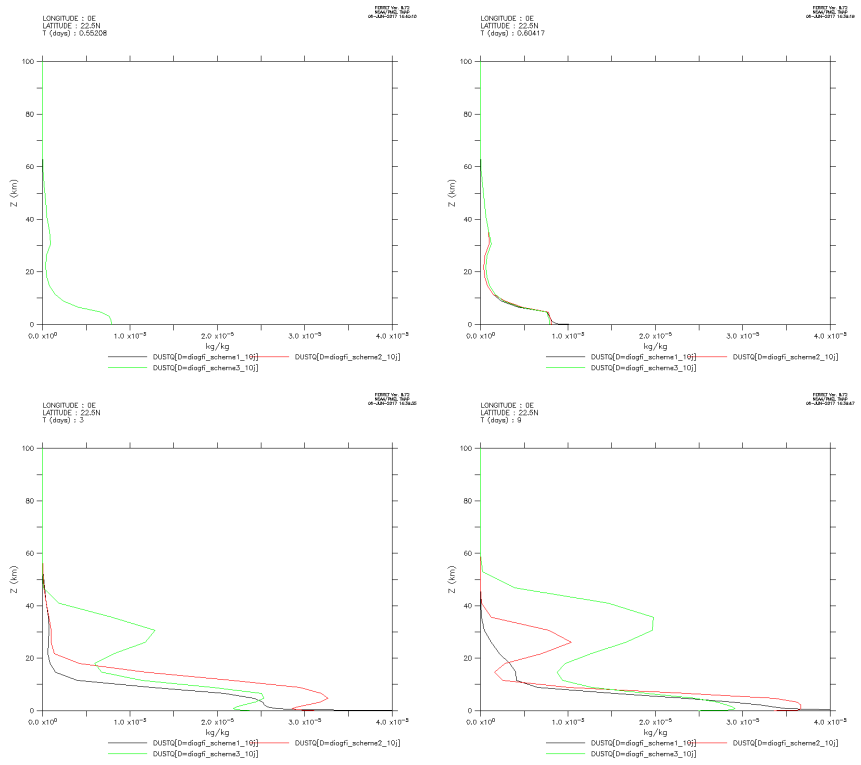

Figure 20: Vertical profiles of dust mass mixing ratios (kg/kg$_{air}$) obtained with the three dust injection schemes. Black line: using scheme 1 (surface injection). Red line: scheme 2 (injection of dust over the first 10km of the atmosphere). Green line: scheme 3 (injection of dust over the first 30km of the atmosphere). FIGURE 20a displays profiles before the injection and 20b at the time step following injection. FIGURES 20c and 20d display profiles at sols 3 and 9.

4.5.4 Comparaison with MCS observations

A better evaluatation of the injection schemes requires inspecting the resulting vertical distribution of dust, compared to observations. FIGURE 21 thus displays density-scaled opacity (km^{-1}) profiles computed by the GCM compared to those observed by MCS at the same location (22.5° N,0° E) and time (15h, Ls=147) during Mars Year 29.
For this particular location and time, only scheme 2 yields a detached dust layer. The agreement is then only qualitative, as quantitatively there is at least a factor 2 between modeled and observed quantities.
Nonetheless, the main result here is that once dust in the GCM is injected in the atmosphere in overall correct quantities and locations, then detached dust layers tend to form and be maintained.

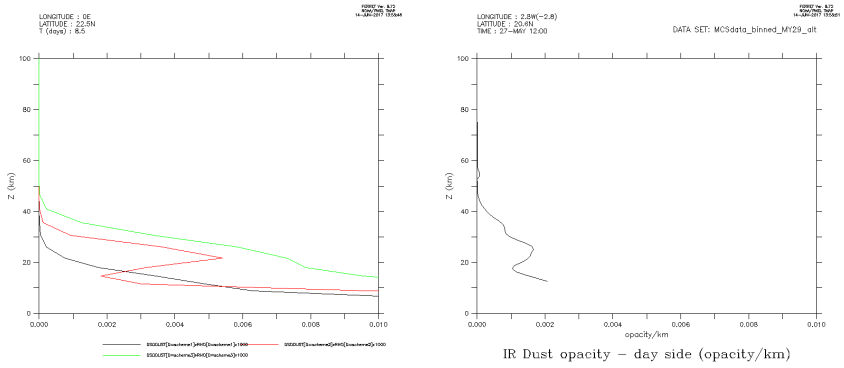

Figure 21: Vertical profiles of density-scaled opacity (dso) for MY29, at Ls=147, LT=15h. a (left figure): Computed in the GCM using the various dust injection schemes: scheme 1 (black line), scheme 2 (red line), scheme 3 (green line). b (right figure): dso from MCD observations [*Heavens et al.*, 2014] at same time and location.

4.6 Conclusions concerning the dust injection schemes

To summarize, the various tests discussed in the previous sections of dust injection based on a prescribed dust scenario have shown that it is overall a feasible way to proceed towards representing a more physical dust cycle at diurnal and annual scales.
The main improvement, compared to the current scheme where dust is continuously rescaled and imposed at every time step (although the dust scenario values are only given once per day) is that the model then exhibits diurnal cycles of dust.
Another key finding is that results are more realistic if dust injections are spread over the daytime rather than done all at once at a given time of day.
It has also been found that if the additional dust is directly injected in altitude (to micmick sub-grid scale processes such as rocket dust storms), then dust detached layers such as those observed by MCS may form.
A couple of caveats to be further investigated have also been identified: Firstly when using the dust injection schemes, dust is transported to polar regions where it remains trapped and accumulates. This most likely would be solved by introducing a parametrization to represent the scavenging of dust by CO_2 clouds that form in the polar region. Secondly some lack of lifting, compared to observation, occurs during the retreat of ploar CO_2 surface ice. This could be improved by allowing some dust lifting to occur even if there is still some surface CO_2 ice present at the surface of a given mesh, to accound for the presence of patches of ice-free areas which will generate local surface temperature inhomogeneities which should generate local thermal breezes capable of lifting available dust.

5 General conclusion

A rocket dust storm parameterization which is based on a parameterization of the dust transport by deep mesoscale convection during rocket dust storms, using global dust scenarios as a quantitative means to evaluate the occurrence of rocket dust storms, has been proposed and implemented in LMD Martian GCM.
Further model developments, regarding the impact of local topographic circulations are beeing studied. The parametrization of the dust lifting by convergence of winds on mountains slopes may complete the full representation of detached dust layers, specially during clear seasons, when the rocket dust storm scheme fails to correlate to observations.
A new scheme of dust injection has also been studied. The future work, which is currently ongoing, will firstly aim at coupling the new dust injection scheme to the rocket dust storm parameterization, and then at completing this parametrization by the further developments regarding the dust lifting by slope convergence.
The full combination and implementation of all these new schemes should significantly improve the representation of the dust cycle, and have direct impact on the global circulation of the Martian LMD GCM. More comparisons to observations of local dust storms will also improve the ad hoc aspects of this parameterization.

References

Basu, S., M. I. Richardson, and R. J. Wilson (2004), Simulation of the Martian dust cycle with the GFDL Mars GCM, *J. Geophys. Res.*, *109*(E18), E11006, doi: 10.1029/2004JE002243.

Basu, S., J. Wilson, M. Richardson, and A. Ingersoll (2006), Simulation of spontaneous and variable global dust storms with the GFDL Mars GCM, *J. Geophys. Res.*, *111*, E09004, doi:10.1029/2005JE002660.

Böing, S. J., A. P. Siebesma, J. D. Korpershoek, and H. J. J. Jonker (2012), Detrainment in deep convection, *Geophys. Res. Lett.*, *39*(20), L21806, doi:10.1029/2012GL053735.

Cantor, B. A. (2007), MOC observations of the 2001 Mars planet-encircling dust storm, *Icarus*, *186*, 60–96, doi:10.1016/j.icarus.2006.08.019.

Cantor, B. A., P. B. James, M. Caplinger, and M. J. Wolff (2001), Martian dust storms: 1999 Mars Orbiter Camera observations, *J. Geophys. Res.*, *106*, 23,653–23,688, doi: 10.1029/2000JE001310.

Cantor, B. A., K. M. Kanak, and K. S. Edgett (2006), Mars Orbiter Camera observations of Martian dust devils and their tracks (September 1997 to January 2006) and evaluation of theoretical vortex models, *J. Geophys. Res.*, *111*(E10), E12002, doi: 10.1029/2006JE002700.

Colaïtis, A., A. Spiga, F. Hourdin, C. Rio, F. Forget, and E. Millour (2013), A thermal plume model for the Martian convective boundary layer, *J. Geophys. Res. Planets*, *118*, 1468–1487, doi:10.1002/jgre.20104.

Conrath, B. J. (1975), Thermal structure of the Martian atmosphere during the dissipation of dust storm of 1971, *Icarus*, *24*, 36–46, doi:10.1016/0019-1035(75)90156-6.

Daerden, F., J. A. Whiteway, L. Neary, L. Komguem, M. T. Lemmon, N. G. Heavens, B. A. Cantor, E. Hébrard, and M. D. Smith (2015), A solar escalator on Mars: Self-lifting of dust layers by radiative heating, *Geophys. Res. Lett.*, *42*, 7319–7326, doi: 10.1002/2015GL064892.

de Rooy, W. C., and A. Siebesma (2010), Analytical expressions for entrainment and detrainment in cumulus convection, *Q. J. R. Meteorol. Soc.*, *136*(650), 1216–1227, doi: 10.1002/qj.640.

de Rooy, W. C., P. Bechtold, K. Fröhlich, C. Hohenegger, H. Jonker, D. Mironov, A. Siebesma, J. Teixeira, and J.-I. Yano (2013), Entrainment and detrainment in cumulus convection: an overview, *Q. J. R. Meteorol. Soc.*, *139*(670), 1–19, doi:10.1002/qj.1959.

Fisher, J. A., M. I. Richardson, C. E. Newman, M. A. Szwast, C. Graf, S. Basu, S. P. Ewald, A. D. Toigo, and R. J. Wilson (2005), A survey of Martian dust devil activity using Mars Global Surveyor Mars Orbiter Camera images, *J. Geophys. Res.*, *110*, E03004, doi:10.1029/2003JE002165.

Forget, F., F. Hourdin, R. Fournier, C. Hourdin, O. Talagrand, M. Collins, S. R. Lewis, P. L. Read, and J.-P. Huot. (1999), Improved general circulation models of the Martian atmosphere from the surface to above 80 km, *J. Geophys. Res.*, *104*, 24,155–24,175, doi:10.1029/1999JE001025.

Forget, F., E. Millour, J.-B. Madeleine, A. Colaitis, A. Spiga, L. Montabone, F. Hourdin, F. Lefèvre, F. Montmessin, F. Gonzalez-Galindo, M. A. Lopez-Valverde, S. R. Lewis, P. R. Read, and D. Mulholland (2011), Back to The Basics: Improving the Prediction of Temperature, Pressure and Winds in the LMD General Circulation Model, in *Mars Atmosphere: Modelling and observation*, edited by F. Forget and E. Millour, pp. 64–67.

Guzewich, S. D., E. R. Talaat, A. D. Toigo, D. W. Waugh, and T. H. McConnochie (2013), High-altitude dust layers on Mars: Observations with the Thermal Emission Spectrometer, *J. Geophys. Res. Planets*, *118*, 1177–1194, doi:10.1002/jgre.20076.

Heavens, N. G., J. L. Benson, D. M. Kass, A. Kleinböhl, W. A. Abdou, D. J. McCleese, M. I. Richardson, J. T. Schofield, J. H. Shirley, and P. M. Wolkenberg (2010), Water ice clouds over the Martian tropics during northern summer, *Geophys. Res. Lett.*, *37*, L18202, doi:10.1029/2010GL044610.

Heavens, N. G., M. I. Richardson, A. Kleinböhl, D. M. Kass, D. J. McCleese, W. Abdou, J. L. Benson, J. T. Schofield, J. H. Shirley, and P. M. Wolkenberg (2011a), Vertical distribution of dust in the Martian atmosphere during northern spring and summer: High-altitude tropical dust maximum at northern summer solstice, *J. Geophys. Res.*, *116*, E01007, doi:10.1029/2010JE003692.

Heavens, N. G., M. I. Richardson, A. Kleinböhl, D. M. Kass, D. J. McCleese, W. Abdou, J. L. Benson, J. T. Schofield, J. H. Shirley, and P. M. Wolkenberg (2011b), The vertical distribution of dust in the Martian atmosphere during northern spring and summer: Observations by the Mars Climate Sounder and analysis of zonal average vertical dust profiles, *J. Geophys. Res.*, *116*, E04003, doi:10.1029/2010JE003691.

Heavens, N. G., D. J. McCleese, M. I. Richardson, D. M. Kass, A. Kleinböhl, and J. T. Schofield (2011c), Structure and dynamics of the Martian lower and middle atmosphere as observed by the Mars Climate Sounder: 2. Implications of the thermal structure and aerosol distributions for the mean meridional circulation, *J. Geophys. Res.*, *116*, E010101, doi:10.1029/2010JE003713.

Heavens, N. G., M. S. Johnson, W. A. Abdou, D. M. Kass, A. Kleinböhl, D. J. McCleese, J. H. Shirley, and R. J. Wilson (2014), Seasonal and diurnal variability of detached dust layers in the tropical martian atmosphere, *J. Geophys. Res. Planets*, *119*, 1748–1774, doi:10.1002/2014JE004619.

Heavens, N. G., B. A. Cantor, P. O. Hayne, D. M. Kass, A. Kleinböhl, D. J. McCleese, S. Piqueux, J. T. Schofield, and J. H. Shirley (2015), Extreme detached dust layers near martian volcanoes: Evidence for dust transport by mesoscale circulations forced by high topography, *Geophys. Res. Lett.*, *42*(10), 3730–3738, doi:10.1002/2015GL064004.

Hourdin, F. (1992), A new representation of the CO_2 15 μm band for a Martian general circulation model, *J. Geophys. Res.*, *97*(E11), 18,319–18,335.

Hourdin, F., and A. Armengaud (1999), Test of a hierarchy of finite-volume schemes for transport of trace species in an atmospheric general circulation model, *Mon. Wea. Rev.*, *127*, 822–837.

Kahre, M. A., J. R. Murphy, and R. M. Haberle (2006), Modeling the Martian dust cycle and surface dust reservoirs with the NASA Ames general circulation model, *J. Geophys. Res.*, *111*, E06008, doi:10.1029/2005JE002588.

Määttänen, A., T. Fouchet, O. Forni, R. Melchiorri, F. Forget, H. Savijarvi, J. P. Bibring, Y. Langevin, B. Gondet, V. Formisano, and M. Giuranna (2009), A study of the properties of a local dust storm with Mars Express OMEGA and PFS data, *Icarus*, *201*(2), 504–516, doi:10.1016/j.icarus.2009.01.024.

Määttänen, A., C. Listowski, F. Montmessin, L. Maltagliati, A. Reberac, L. Joly, and J.-L. Bertaux (2013), A complete climatology of the aerosol vertical distribution on Mars from MEx/SPICAM UV solar occultations, *Icarus*, *223*, 892–941, doi:10.1016/j.icarus.2012.12.001.

Madeleine, J.-B., F. Forget, E. Millour, L. Montabone, and M. J. Wolff (2011), Revisiting the radiative impact of dust on Mars using the LMD Global Climate Model, *J. Geophys. Res.*, *116*, E11010, doi:10.1029/2011JE003855.

Madeleine, J.-B., F. Forget, E. Millour, T. Navarro, and A. Spiga (2012), The influence of radiatively active water ice clouds on the Martian climate, *Geophys. Res. Lett.*, *39*, L23202, doi:10.1029/2012GL053564.

Malin, M. C., B. A. Cantor, M. R. Kennedy, D. E. Shean, and T. N. Harrison (2008), Mro marci weather report for the week of 20 october 2008 - 26 october 2008, *Malin Space Science Systems Captioned Image Release*, *MSSS-56*.

McCleese, D. J., J. T. Schofield, F. W. Taylor, S. B. Calcutt, M. C. Foote, D. M. Kass, C. B. Leovy, D. A. Paige, P. L. Read, and R. W. Zurek (2007), Mars Climate Sounder: An investigation of thermal and water vapor structure, dust and condensate distributions in the atmosphere, and energy balance of the polar regions, *J. Geophys. Res.*, *112*, E05S06, doi:10.1029/2006JE002790.

McCleese, D. J., N. G. Heavens, J. T. Schofield, W. A. Abdou, J. L. Bandfield, S. B. Calcutt, P. G. J. Irwin, D. M. Kass, A. Kleinböhl, S. R. Lewis, D. A. Paige, P. L. Read, M. I. Richardson, J. H. Shirley, F. W. Taylor, N. Teanby, and R. W. Zurek (2010), Structure and dynamics of the Martian lower and middle atmosphere as observed by the Mars Climate Sounder: Seasonal variations in zonal mean temperature, dust, and water ice aerosols, *J. Geophys. Res.*, *115*, E12016, doi:10.1029/2010JE003677.

Montabone, L., F. Forget, E. Millour, R. Wilson, S. Lewis, B. Cantor, D. Kass, A. Kleinböhl, M. Lemmon, M. Smith, and M. Wolff (2015), Eight-year climatology of dust optical depth on mars, *Icarus*, *251*, 65–95, doi:10.1016/j.icarus.2014.12.034.

Montmessin, F., F. Forget, P. Rannou, M. Cabane, and R. M. Haberle (2004), Origin and role of water ice clouds in the Martian water cycle as inferred from a general circulation model, *J. Geophys. Res.*, *109*, E10004, doi:10.1029/2004JE002284.

Mulholland, D. P., P. L. Read, and S. R. Lewis (2013), Simulating the interannual variability of major dust storms on Mars using variable lifting thresholds, *Icarus*, *223*, 344–358, doi:10.1016/j.icarus.2012.12.003.

Mulholland, D. P., A. Spiga, C. Listowski, and R. P. L. (2015), An assessment of the impact of local processes on dust lifting in martian climate models, *Icarus*, *252*, 212–227, doi:10.1016/j.icarus.2015.01.017.

Navarro, T., F. Forget, E. Millour, and S. J. Greybush (2014a), Detection of detached dust layers in the Martian atmosphere from their thermal signature using assimilation, *Geophys. Res. Lett.*, *41*, 6620–6626, doi:10.1002/2014GL061377.

Navarro, T., J.-B. Madeleine, F. Forget, A. Spiga, E. Millour, F. Montmessin, and A. Määttänen (2014b), Global Climate Modeling of the Martian water cycle with improved microphysics and radiatively active water ice clouds, *J. Geophys. Res. Planets*, *119*, 1479–1495, doi:10.1002/2013JE004550.

Newman, C. E., and M. I. Richardson (2015), The impact of surface dust source exhaustion on the martian dust cycle, dust storms and interannual variability, as simulated by the MarsWRF general circulation model, *Icarus*, *257*, 47 – 87, doi:10.1016/j.icarus.2015.03.030.

Newman, C. E., S. R. Lewis, P. L. Read, and F. Forget (2002), Modeling the Martian dust cycle 2. Multiannual radiatively active dust transport simulations, *J. Geophys. Res.*, *107*(E12), 5124, doi:10.1029/2002JE001920.

Rafkin, S. C. R. (2009), A positive radiative-dynamic feedback mechanism for the maintenance and growth of Martian dust storms, *J. Geophys. Res.*, *114*, E01009, doi: 10.1029/2008JE003217.

Rafkin, S. C. R. (2012), The potential importance of non-local, deep transport on the energetics, momentum, chemistry, and aerosol distributions in the atmospheres of Earth, Mars, and Titan, *Planet. Space Sci.*, *60*, 147–154, doi:10.1016/j.pss.2011.07.015.

Rafkin, S. C. R., M. R. V. Sta. Maria, and T. I. Michaels (2002), Simulation of the atmospheric thermal circulation of a martian volcano using a mesoscale numerical model, *Nature*, *419*, 697–699.

Smith, M. D., M. J. Wolff, R. T. Clancy, A. Kleinböhl, and S. L. Murchie (2013), Vertical distribution of dust and water ice aerosols from CRISM limb-geometry observations, *J. Geophys. Res. Planets*, *118*, 321–334, doi:10.1002/jgre.20047.

Spiga, A. (2011), Elements of comparison between Martian and terrestrial mesoscale meteorological phenomena: Katabatic winds and boundary layer convection, *Planet. Space Sci.*, *59*, 915–922, doi:10.1016/j.pss.2010.04.025.

Spiga, A., J. Faure, J.-B. Madeleine, A. Määttänen, and F. Forget (2013), Rocket dust storms and detached dust layers in the Martian atmosphere, *J. Geophys. Res. Planets*, *118*, 746–767, doi:10.1002/jgre.20046.

Van Leer, B. (1977), Towards the ultimate conservative difference scheme : IV. a new approach to numerical convection, *J. Computational Phys.*, *23*, 276–299.

Wang, H., and M. I. Richardson (2015), The origin, evolution, and trajectory of large dust storms on mars during mars years 24-30 (1999-2011), *Icarus*, *251*, 112–127, doi: 10.1016/j.icarus.2013.10.033.

Wolff, M. J., M. D. Smith, R. T. Clancy, N. Spanovich, B. A. Whitney, M. T. Lemmon, J. L. Bandfield, D. Banfield, A. Ghosh, G. Landis, P. R. Christensen, J. F. Bell, and S. W. Squyres (2006), Constraints on dust aerosols from the Mars Exploration Rovers using MGS overflights and Mini-TES, *J. Geophys. Res.*, *111*, E12S17, doi: 10.1029/2006JE002786.

Wolff, M. J., M. D. Smith, R. T. Clancy, R. Arvidson, M. Kahre, F. Seelos, S. Murchie, and H. Savijärvi (2009), Wavelength dependence of dust aerosol single scattering albedo as observed by the Compact Reconnaissance Imaging Spectrometer, *J. Geophys. Res.*, *114*, E00D04, doi:10.1029/2009JE003350.

Ye, Z. J., M. Segal, and R. A. Pielke (1990), A comparative study of daytime thermally induced upslope flow on Mars and earth, *J. Atmos. Sci.*, *47*, 612–628.